



NRL/FR/7100--02-10,042

Broadband Models for Predicting Bistatic Bottom, Surface, and Volume Scattering Strengths

ROGER C. GAUSS
ROBERT F. GRAGG
DANIEL WURMSER
JOSEPH M. FIALKOWSKI

*Acoustic Systems Branch
Acoustics Division*

REDWOOD W. NERO
*Acoustic Simulation, Measurements, and Tactics Branch
Acoustics Division*

September 30, 2002

Approved for public release; distribution is unlimited.

REPORT DOCUMENTATION PAGE				Form Approved OMB No. 0704-0188	
Public reporting burden for this collection of information is estimated to average 1 hour per response, including the time for reviewing instructions, searching existing data sources, gathering and maintaining the data needed, and completing and reviewing this collection of information. Send comments regarding this burden estimate or any other aspect of this collection of information, including suggestions for reducing this burden to Department of Defense, Washington Headquarters Services, Directorate for Information Operations and Reports (0704-0188), 1215 Jefferson Davis Highway, Suite 1204, Arlington, VA 22202-4302. Respondents should be aware that notwithstanding any other provision of law, no person shall be subject to any penalty for failing to comply with a collection of information if it does not display a currently valid OMB control number. PLEASE DO NOT RETURN YOUR FORM TO THE ABOVE ADDRESS.					
1. REPORT DATE (DD-MM-YYYY) September 30, 2002		2. REPORT TYPE		3. DATES COVERED (From - To)	
4. TITLE AND SUBTITLE Broadband Models for Predicting Bistatic Bottom, Surface, and Volume Scattering Strengths				5a. CONTRACT NUMBER	
				5b. GRANT NUMBER	
				5c. PROGRAM ELEMENT NUMBER	
6. AUTHOR(S) Roger C. Gauss, Robert F. Gragg, Redwood W. Nero, ¹ Daniel Wurmser, and Joseph M. Fialkowski ²				5d. PROJECT NUMBER	
				5e. TASK NUMBER	
				5f. WORK UNIT NUMBER	
7. PERFORMING ORGANIZATION NAME(S) AND ADDRESS(ES) Naval Research Laboratory, Code 7100 4555 Overlook Avenue, SW Washington, DC 20375-5320				8. PERFORMING ORGANIZATION REPORT NUMBER NRL/FR/7100--02-10,042	
9. SPONSORING / MONITORING AGENCY NAME(S) AND ADDRESS(ES)				10. SPONSOR / MONITOR'S ACRONYM(S)	
				11. SPONSOR / MONITOR'S REPORT NUMBER(S)	
12. DISTRIBUTION / AVAILABILITY STATEMENT Approved for public release; distribution is unlimited.					
13. SUPPLEMENTARY NOTES ¹ NRL-SSC ² Work performed while at Planning Systems, Inc., Reston Virginia					
14. ABSTRACT Multistatic active system performance can be driven by reverberation from the ocean boundaries and biologies. Providing accurate sonar performance predictions of reverberation, in turn, relies on providing accurate estimates of bistatic scattering strengths. This report presents new three-dimensional models that provide physics-based estimates of the dependence of scattering strength on the incident and scattered grazing angles, the bistatic angle, the acoustic frequency (10 to 10000 Hz), and physical descriptors of the environment (such as bottom properties for the bottom model, wind speed for the surface model, and fish properties for the volume model). The bottom model describes scattering from rough, elastic interfaces, while the surface model describes scattering from both the rough air-sea interface and subsurface bubbles. The volume models describe scattering from dispersed bladdered fish, including boundary-interference effects. For all, parameter studies along with data-model comparisons demonstrate the importance of using physics-based scattering models to describe the complex acoustic interaction processes at the ocean boundaries. These broadband models can enhance sonar performance prediction capabilities through their inclusion as submodels in both active performance/reverberation models (such as the Comprehensive Acoustic System Simulation (CASS) or the Bistatic Range-dependent Active System Performance (BiRASP) models) and inverse algorithms (such as environmentally adaptive techniques).					
15. SUBJECT TERMS Bottom scattering; Surface scattering; Volume scattering; Underwater acoustics					
16. SECURITY CLASSIFICATION OF:			17. LIMITATION OF ABSTRACT UL	18. NUMBER OF PAGES 50	19a. NAME OF RESPONSIBLE PERSON Roger C. Gauss
a. REPORT Unclassified	b. ABSTRACT Unclassified	c. THIS PAGE Unclassified			19b. TELEPHONE NUMBER (include area code) (202) 767-3524

CONTENTS

1. INTRODUCTION	1
2. DEFINITIONS	2
3. INTERFACE SCATTERING MODELS	3
Theoretical Formulation	4
Numerical Implementation	5
Ocean Bottom Model	6
Ocean Surface Model	7
4. BOTTOM INTERFACE SCATTERING	8
Geophysical Parameter Values	8
Model Illustrations	9
Comments	18
5. VOLUME SCATTERING	18
Single Fish Swimbladder Model	18
Layer of Fish Swimbladder Model	22
Fish Near Boundaries	22
Model Illustrations	24
Comments	30
6. SURFACE SCATTERING	30
Data Sources	31
Interface Scattering Model	31
Bubble-Cloud Scattering Model	32
Model-Model Comparisons	34
Simplified SSS Model	34
Model Illustrations	34
Comments	38
7. CONCLUSIONS	39
General Interface Scattering	40
Bottom Interface Scattering	40
Volume Scattering	40
Surface Scattering	41

Issues	41
Recommendations	43
ACKNOWLEDGMENTS	43
REFERENCES	43

BROADBAND MODELS FOR PREDICTING BISTATIC BOTTOM, SURFACE, AND VOLUME SCATTERING STRENGTHS*

1. INTRODUCTION

For a low-frequency (50 to 1000 Hz) or mid-frequency (1 to 10 kHz) operational active sonar, scattering from the ocean boundaries and biotics, coupled with propagation conditions, can severely limit the detectability of returns from features of interest. Furthermore, reverberation levels can vary dramatically, depending on the local geology, oceanography, and biology. Hence, making accurate predictions of active sonar performance will, in turn, depend on finding suitable empirical or physics-based models that accurately describe the scattering. This paper presents broadband, three-dimensional (3D), ocean bottom, surface, and volume (fish) scattering models that should not only improve the robustness and accuracy of sonar performance predictions of multistatic reverberation, but also provide new insights as to the significance of each scattering mechanism.

Bottom scatter is generally the dominant interference source for active systems in littoral waters. However, it is a poorly understood combination of scattering from rough interfaces (water-sediment, sediment-sediment, sediment-basement) and the sediment volume. This is a result of both the complexity of the ocean bottom and the difficulty of acquiring in situ environmental inputs to the accuracy required by models.

Surface scattering is caused by the interaction of acoustic energy with environmental features at or near the ocean surface. The dynamic nature of the air-sea boundary interaction zone complicates this process [1]. When wave breaking is significant, air becomes entrained in the form of subsurface bubbles. Under these conditions, both the rough air-sea interface and bubble clouds may contribute to the acoustic scattering.

Volume scattering at low- and mid-frequencies is primarily caused by acoustic interaction with fish swimbladders. General scattering models for dispersed bladdered fish (incoherent sum of scattering from individual fish) have been developed [2] that, when coupled with fish-distribution algorithms, provide regional predictions of mean volume scattering [3]. (Fish distribution and behavior are linked to oceanographic variables such as ocean temperature, mixed-layer depths and topography that can be used to advantage to predict fish distributions.) When fish school, as is common in shallow water, the scattering picture is more complicated. The Naval Research Laboratory (NRL) has developed a scattering model for small-sized fish schools that includes all orders of multiple scattering interactions between the fish (with the aggregate scattering field calculated by coherent summation) [4]. Another set of complications arises when fish are in the presence of reflecting boundaries [5]. This paper extends the free-field dispersed-fish model by incorporating boundary-interference effects for both the ocean surface and bottom.

Recent broadband scattering measurements conducted by NRL under the Space and Naval Warfare Systems Command's Critical Sea Test (CST) program [6] (1988-1996) and the Office of Naval Research's Littoral Warfare Advanced Development (LWAD) project [7] (1996-present), have helped to distinguish the important scattering mechanisms and determine the environmental conditions for which each mechanism makes significant contributions. Using a variety of systems and waveforms, NRL made direct-path measurements of bottom, surface, and volume backscattering characteristics for a range of frequencies and environmental conditions in both the open ocean and shallow water. These measured acoustic quantities have been correlated to archival bottom properties, environmental measurements of the air-sea boundary conditions (such as wind speed, wave spectra, and bubble parameters), and in situ assessments of biological quantities (such as fish densities and sizes).

Manuscript approved October 2, 2001.

*This report appeared in the *U.S. Navy Journal of Underwater Acoustics*, Vol. 51, No. 3, July 2001.

In conjunction with these scattering measurements, NRL has been developing both empirical and physics-based models of scattering strength, with an emphasis on generating formulas suitable for inclusion as submodels in both active performance/reverberation models and inverse algorithms (such as environmentally adaptive techniques). To this end, this paper describes the latest versions of these models for estimating the dependence of scattering strength on the incident and scattered grazing angles, the bistatic angle, the acoustic frequency, biological descriptors of the fish, and physical descriptors of the environment. After a few definitions, the paper begins with a discussion of 3D interface-scattering models, applicable to both ocean boundaries. Then, discussed in turn, are the new models for calculating the scattering strengths of the bottom interface; dispersed bladdered fish near boundaries; and the sea surface (air-sea interface and bubble clouds). We conclude with a few comments and recommendations.

2. DEFINITIONS

Scattering strength (in dB) is defined by

$$SS = 10 \cdot \log_{10} \sigma, \quad (1)$$

where σ is the scattering cross section per unit area (per unit solid angle), a dimensionless quantity. Scattering strength represents a mean far-field (plane-wave) quantity.

The scattering geometry adopted in this paper follows Jackson [8] and is illustrated in Fig. 1 for the ocean bottom. (For the ocean surface, the geometry is inverted, so that positive z corresponds to depth below the surface.) Here, \mathbf{k} and \mathbf{q} are the incoming and outgoing wavevectors, respectively, and define the incident grazing angle θ_{inc} and the scattered grazing angle θ_{scat} . The bistatic angle ϕ_{bi} is defined as the difference in azimuth between the incident and scattered directions. (There is only one bistatic angle; the scattering statistics of the interface roughness and volume heterogeneities are assumed to be locally transversely isotropic.) This in turn implies SS will be an even function of ϕ_{bi} , i.e., $SS(\theta_{inc}, \theta_{scat}, \phi_{bi}) = SS(\theta_{inc}, \theta_{scat}, -\phi_{bi})$.

With these definitions, we have $0 < \theta_{inc} \leq 90^\circ$, $0 < \theta_{scat} < 180^\circ$, and $-180^\circ < \phi_{bi} \leq 180^\circ$. Bistatic angles of $\pm 180^\circ$ correspond to the backscatter direction, and a bistatic angle of 0° with $\theta_{inc} = \theta_{scat}$ corresponds to the specular direction. (Figure 1 also shows that $SS(\theta_{inc}, \theta_{scat}, \phi_{bi}) = SS(\theta_{inc}, 180^\circ - \theta_{scat}, \phi_{bi} \pm 180^\circ)$, so that $\phi_{bi} = \pm 180^\circ$ with $\theta_{scat} = 180^\circ - \theta_{inc}$ also correspond to specular.) All the scattering strength models will satisfy reciprocity in that $SS(\theta_{inc}, \theta_{scat}, \phi_{bi}) = SS(\theta_{scat}, \theta_{inc}, \phi_{bi})$.

In terms of angles, the incident and scattered wavevectors can be written as

$$\mathbf{k} = k_0 (\cos \theta_{inc} \hat{\mathbf{x}} - \sin \theta_{inc} \hat{\mathbf{z}}), \quad (2)$$

$$\mathbf{q} = k_0 (\cos \theta_{scat} \cos \phi_{bi} \hat{\mathbf{x}} + \cos \theta_{scat} \sin \phi_{bi} \hat{\mathbf{y}} + \sin \theta_{scat} \hat{\mathbf{z}}), \quad (3)$$

where $k_0 = 2\pi f/c_0$ is the acoustic wavenumber, with f the acoustic frequency and c_0 the speed of sound in bubble-free seawater at the interface. Later expressions for the interface scattering cross sections will depend on the horizontal and vertical magnitudes of the difference of these two wavevectors. Defining $\mathbf{k} - \mathbf{q} = (Q_h, Q_z)$, their magnitudes can be expressed in terms of the scattering angles:

$$|Q_h| = k_0 \sqrt{\cos^2 \theta_{inc} + \cos^2 \theta_{scat} - 2 \cos \theta_{inc} \cos \theta_{scat} \cos \phi_{bi}}, \quad (4)$$

$$Q_z = -k_0 (\sin \theta_{inc} + \sin \theta_{scat}). \quad (5)$$

MKS units are used throughout this paper.

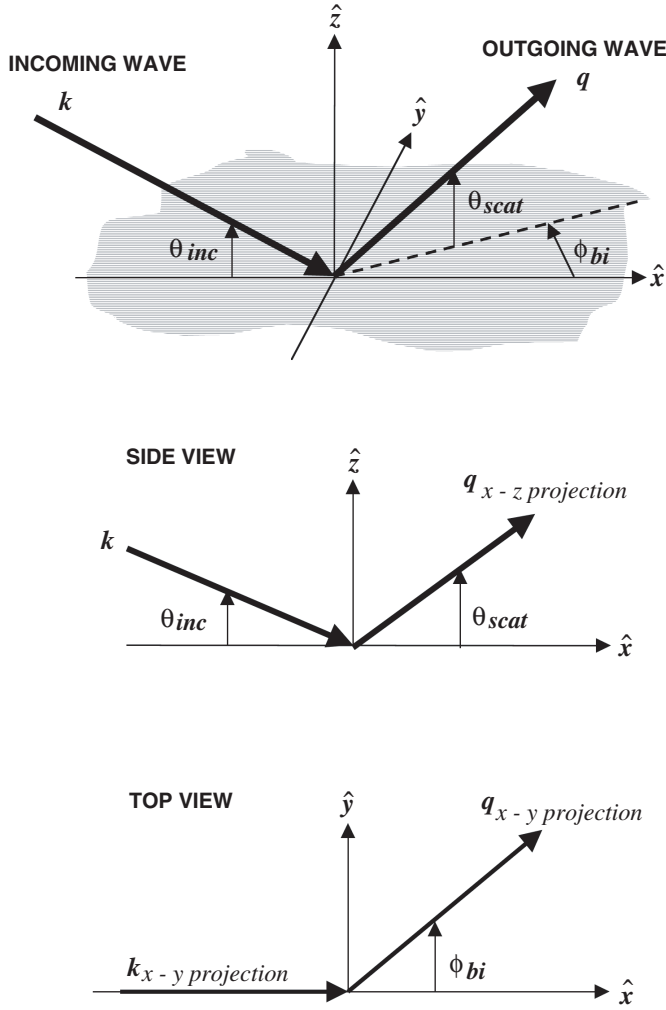


Fig. 1 — Definition of scattering angles: 3D, side, and top views, as illustrated for the ocean bottom

3. INTERFACE SCATTERING MODELS

A variety of models have been applied to sound scattering by rough ocean boundaries, such as first-order (Born approximation) and higher-order perturbation theories, and composite-roughness models. For this paper, the small slope formalism of Voronovich [9-11], as adapted for the ocean surface by Dashen et al. [12] and elastic seafloors by Wurmser [13], is used to predict the contributions of the boundary interfaces to the total scattering. This lowest-order small-slope approximation (SSA) models interface scattering strength to all orders in surface height h , and through first order in the derivatives of h (surface slope). Using the local small-slope approximation instead of the standard first-order perturbation approximation increases the accuracy of the prediction at the expense of a modest increase in numerical complexity [14].

Bottom and surface roughness are taken to be Gaussian random processes, each described by a two-parameter, isotropic, 2D roughness spectral density of the form [8,12]

$$W(\mathbf{Q}_h) = \frac{w_2}{(h_0 |\mathbf{Q}_h|)^{\gamma_2}}, \quad (6)$$

with $\gamma_2 \in (2, 4)$, $|\mathbf{Q}_h|$ given by Eq. (4), and h_0 a normalizing reference distance of 1 m. (Each subscript “2” refers to the boundary relief being described by a 2D random process [8].) The units of w_2 are m^4 . Higher values of γ_2 in the given range correspond to a weaker frequency dependence.

As is standard, the coherent specular component is removed in this treatment of rough surface scattering theory. Following Jackson [8], these interface-scattering models assume that *all* scattered energy is incoherent. Hence, it would be a mistake to add a coherent reflected wave to these models, as conservation of energy would then be violated. This is an artifact of the spectrum given in Eq. (6). For such spectra, there is no small-wavenumber (i.e., large-scale) cut-off, and so the surface remains rough even at the largest scales. Specular reflection is ordinarily generated because the surface flattens out at the largest scales. On the other hand, if the surface has very little large-scale roughness, then there will be a sharp peak in σ_{int} in the specular direction, with its magnitude and width such as to give the correct energy flux. Hence, issues related to the large scales (i.e., small wavenumbers), most notably the lack of a low-wavenumber cut-off, generally affect scattering near the specular direction. (We are working on improvements to these models, but a fundamental problem remains with the ocean bottom since there is no general procedure for determining the cut-off.)

Because the model development is applicable to both the ocean bottom and surface, we begin with the general, lowest-order SSA formulation and discuss its numerical implementation before specializing to specific boundaries. These developments are applicable to the full 3D problem.

Theoretical Formulation

The SSA result for the noncoherent component of the scattering cross section per unit area (per unit solid angle) for a random, rough interface has the form [12]

$$\sigma_{int} = \frac{1}{8\pi} \left| \frac{\beta}{|\mathbf{Q}_h| Q_z} \right|^2 \cdot I, \quad (7)$$

where β is an algebraic form that depends on the boundary conditions prevailing at the interface, I is an integral involving the spatial spectrum of the roughness, and $|\mathbf{Q}_h|$ and Q_z are given by Eqs. (4) and (5), respectively. (Equation (7) is similar in form to Eq. (38) of Jackson et al. [15] and Eq. (11) of Williams and Jackson [16], except that the coefficient in front of the integral is a small-slope approximation while theirs are Kirchhoff approximations.)

With $\nu \equiv (\gamma_2 - 2)/2$, and thus $\nu \in (0, 1)$, the integral in Eq. (7) is [17-18]

$$I(\alpha) = \int_0^\infty J_0(y) y B(y, \alpha) dy, \quad \text{where } B(y, \alpha) = \exp(-\alpha y^{2\nu}), \quad (8)$$

J_0 is the zeroth-order Bessel function of the first kind, and α is given by

$$\alpha = \frac{(h_{rms} Q_z)^2}{(2h_0 |\mathbf{Q}_h|)^{2\nu}} \frac{\Gamma(1-\nu)}{\Gamma(1+\nu)}, \quad (9)$$

with the mean-square roughness h_{rms}^2 defined by

$$h_{rms}^2 = \frac{\pi w_2}{h_0^2 \nu}. \quad (10)$$

(In the derivation of the lowest-order SSA, a finite cut-off spectrum is used. However, as a result of cancellations during the procedure, the finite cut-off disappears and W effectively assumes the pure power law form described by Eq. (6).)

Assuming the sound speeds—both the real and imaginary (attenuation) parts—are frequency-independent, then the only frequency dependence in σ_{int} comes from the parameter α , which under these circumstances is

proportional to $f^{2(1-\nu)} = f^{4-\gamma_2}$ [18]. In this case, the only environmental parameter that influences the frequency dependence is the boundary roughness spectral exponent γ_2 . On the other hand, once the real or imaginary part of a sound speed acquires a dependence on frequency, then α , β , and of course σ_{int} all acquire complicated frequency dependencies.

Numerical Implementation

While the integral in Eq. (7) is well-defined, it is not easily evaluated due to an oscillating integrand that decays at a highly variable rate. This difficulty is compounded by the requirement that $I(\alpha)$ be evaluated over a wide range of α (a wide range of grazing angles). Two approaches have been developed to numerically implement Eq. (7). Together, they provide a recipe for calculating σ_{int} that covers most γ_2 of practical interest.

Two-Series Approach

The first approach [19] uses a series representation of $J_0(y)$ to perform the integration of $I(\alpha)$ term-wise for large α , and a second series for $B(y, \alpha)$ to do the same for small α . (The power law form of the argument of the exponential in $B(y, \alpha)$ occurs because the autocorrelation function for the surface height function has been expanded to first order. Numerically, this form is particularly useful because at this order, the finite cut-off of the surface spectrum disappears, and because there are no general rules for specifying the spectral peak for the ocean bottom.) With this approach, the integral of Eq. (8) is approximated as a pair of easy-to-evaluate sums [17-19].

$$I(\alpha) \approx \frac{2}{\nu} \sum_{n=1}^{\hat{n}_U} (-)^{n+1} \frac{\Gamma(n/\nu)}{\Gamma^2(n)} \frac{1}{(4\alpha^{1/\nu})^n} \quad \hat{\alpha} < \alpha \quad (11a)$$

$$\approx \frac{2}{\pi} \sum_{n=1}^{\hat{n}_L} (-)^{n+1} \sin(\pi n \nu) \frac{\Gamma^2(n\nu+1)}{\Gamma(n+1)} (4^\nu \alpha)^n \quad \alpha \leq \hat{\alpha}. \quad (11b)$$

Equation (11) is valid for $\nu \in (0.5, 1) \Leftrightarrow \gamma_2 \in (3, 4)$. For $\alpha \leq \hat{\alpha}$, $\hat{n}_L = 10$ works for all valid values of γ_2 . For $\hat{\alpha} < \alpha$, the values of both $\hat{\alpha}$ and \hat{n}_U depend on the value of the spectral exponent γ_2 : it has been determined [19] that the integral sum in Eq. (11a) calculates the integral $I(\alpha)$ accurately to three significant figures for the $\hat{\alpha}$ and \hat{n}_U given in Table 1 for nine values of $\gamma_2 \in (3, 4)$.

It is straightforward to show that, when only the first term of Eq. (11b) is used, Eq. (7) becomes

$$\sigma_{int} \approx \left| \frac{\beta}{2} \right|^2 \frac{w_2}{(h_0 |\mathbf{Q}_h|)^{2(\nu+1)}} = \left| \frac{\beta}{2} \right|^2 W(\mathbf{Q}_h), \quad (12)$$

which is the result from first-order perturbation theory.

Table 1 — Sum-Transition Parameter Values for Eq. (11a)

γ_2	3.1	3.2	3.3	3.4	3.5	3.6	3.7	3.8	3.9
$\hat{\alpha}$	0.39	0.25	0.20	0.15	0.12	0.08	0.05	0.03	0.025
\hat{n}_U	6545	610	155	93	62	60	62	67	54

Rational-Function Approach

To obtain an expression for $I(\alpha)$ that extends its range of validity to all $v_2 \in [0.2, 0.95]$, a second numerical procedure has been developed [20-21]. This approach uses expansion (11b) with $\hat{n}_L = 40$, and replaces expansion (11a) by exploiting a rational-function approximation of $B(y, \alpha)$ for a particular reference value of α . This transition value $\hat{\alpha}$ depends on γ_2 via the empirical relationship [18]

$$\log_{10} \hat{\alpha} = -1.7567\gamma_2 + 4.4926, \quad (13)$$

and replaces the discrete $\hat{\alpha}$'s of Table 1.

Defining $x = y^2$, the rational-function approximation of order $[N, D]$, with $D > N$, is

$$B(\sqrt{x}, \hat{\alpha}) \approx \frac{1 + n_1 x + \dots + n_N x^N}{1 + d_1 x + \dots + d_D x^D}. \quad (14)$$

With the numerator and denominator polynomials factored, the right-hand side of Eq. (14) becomes $(1 - x/z_1) \dots (1 - x/z_N)/(1 - x/p_1) \dots (1 - x/p_D)$ in terms of the zeros z_i and poles p_j . Any poles that happen to lie on the positive real axis will degrade the quality of the approximation. These are dealt with using a splitting technique that replaces the pole $p > 0$ with a pair of rotated poles ($pe^{+i\delta}$, $pe^{-i\delta}$) and also introduces a new zero $z = p/(2 \cos \delta - 1)$. Each such replacement increases both N and D by unity, leaving $D - N$ unchanged. The rotation angle δ is arbitrary except for the requirement $\delta > 60^\circ$ to prevent $z > 0$. (We use $\delta = 90^\circ$.) After the rotation of any positive poles, the factored form of Eq. (14) can be converted to the partial-fraction form, $B(\sqrt{x}, \hat{\alpha}) = \sum_{j=1}^D r_j / (x - p_j)$, involving the modified poles and the residues r_j . For general α , the exponential factor can be written $B(y, \alpha) = B(sy, \hat{\alpha})$ in terms of the scale factor $s = (\alpha / \hat{\alpha})^{1/2v}$ so that $B(y, \alpha) = \sum_{j=1}^D r_j / ((sy)^2 - p_j)$. With this, Eq. (8) reduces to a sum of tabulated integrals, and the final outcome is

$$I(\alpha) \approx \sum_{j=1}^D \frac{r_j}{s^2} K_0 \left(\frac{\sqrt{-p_j}}{s} \right), \quad (15)$$

where K_0 is the zeroth-order modified Bessel function of the second kind. In practice, one can use $[N, D] = [6, 9]$ in all cases [18].

To apply these equations to the ocean bottom and surface, we need to specify the appropriate boundary conditions. This is done in the next two subsections.

Ocean Bottom Model

Wurmser [13] has derived β for the general case of a fluid/elastic-solid interface. In this case, the following additional environmental parameters are required beyond c_0 :

- ρ_{bot} = ratio of solid mass density to the fluid mass density
- c_p = complex sound speed of the p -wave in the solid (compressional speed and attenuation)
- c_s = complex sound speed of the s -wave in the solid (shear speed and attenuation).

The complex acoustic wavenumbers corresponding to c_p and c_s are, respectively:

$$k_p = 2\pi f / c_p \quad \text{and} \quad k_s = 2\pi f / c_s. \quad (16)$$

We now define three pairs of general functions that will be used in constructing β :

$$\begin{aligned}
 a_j(\theta_j; \rho_{bot}, k_0, k_p, k_s) &\equiv \rho_{bot} \frac{k_0 \sin \theta_j}{P_j} \left[1 - \frac{4k_0^2 \cos^2 \theta_j S_j (S_j - P_j)}{k_s^4} \right], \\
 b_j(\theta_j; \rho_{bot}, k_0, k_p, k_s) &\equiv \rho_{bot} \frac{k_0 \sin \theta_j}{P_j} \left(1 - \frac{2k_0^2 \cos^2 \theta_j}{k_s^2} \right), \\
 \xi_j(\theta_j; k_0, k_p, k_s) &\equiv \frac{k_0 \sin \theta_j}{k_s^2 P_j} [(S_j - P_j)^2 - k_p^2],
 \end{aligned} \tag{17}$$

where

$$\begin{aligned}
 P_j &\equiv \sqrt{k_p^2 - k_0^2 \cos^2 \theta_j}, \quad S_j \equiv \sqrt{k_s^2 - k_0^2 \cos^2 \theta_j}, \\
 \text{with } \theta_1 &= \theta_{inc} \text{ and } \theta_2 = \theta_{scat}.
 \end{aligned} \tag{18}$$

Finally, we note from Eqs. (2) and (3) that

$$[\mathbf{k}_h \cdot \mathbf{q}_h] = k_0^2 \cos \theta_{inc} \cos \theta_{scat} \cos \phi_{bi}. \tag{19}$$

With these definitions, we are now ready to write down the expression for β :

$$\begin{aligned}
 \beta(\theta_{inc}, \theta_{scat}, \phi_{bi}; \rho_{bot}, k_0, k_s, k_p) &= \frac{1}{(a_1 + 1)(a_2 + 1)} \left\{ 4(1 - \rho_{bot}) ([\mathbf{k}_h \cdot \mathbf{q}_h] \xi_1 \xi_2 - k_0^2 \sin \theta_{inc} \sin \theta_{scat}) \right. \\
 &\quad \left. + \frac{8\rho_{bot}}{k_s^2} [\mathbf{k}_h \cdot \mathbf{q}_h]^2 \xi_1 \xi_2 - 4[\mathbf{k}_h \cdot \mathbf{q}_h] (a_1 - \xi_1)(a_2 - \xi_2) + 4k_0^2 a_1 a_2 + \frac{2k_s^2}{\rho_{bot}} (a_1 - b_1)(a_2 - b_2) - \frac{4k_p^2}{\rho_{bot}} b_1 b_2 \right\}.
 \end{aligned} \tag{20}$$

Thus, for this model, σ_{int}^{bot} depends on eight environmental parameters: c_0 and seven geophysical parameters: ρ_{bot} , $\text{Re}\{c_p\}$, $\text{Im}\{c_p\}$, $\text{Re}\{c_s\}$, $\text{Im}\{c_s\}$, w_2 , and γ_2 .

It should be noted that this 3D formulation of σ_{int}^{bot} is for a fluid-solid interface (and reduces to the fluid-fluid case in the appropriate limits). However, for most cases this SSA formula will handle not only the water-sediment interface, but sediment-sediment and sediment-(acoustic)-basement interfaces as well. For these latter scenarios, the overlying sediment basically acts as a fluid, so that the above expressions would still hold for such cases as a sand-limestone interface. (For expressions capable of handling solid-solid interfaces, see Ref. 13.)

Ocean Surface Model

Calculating β for the sea surface is much simpler (Dirichlet boundary conditions). The result is [12]

$$\beta = -4k_0^2 \sin \theta_{inc} \sin \theta_{scat}. \tag{21}$$

(Note that, in contrast to the ocean bottom case, β for the ocean surface does not depend on the bistatic angle ϕ_{bi} .)

The sea surface contains many scales of roughness, from the long gravity waves (“swell”) to the short capillary waves. While a variety of directional surface-roughness spectral models are available [22], for this paper we assume an isotropic spectral model (Eq. (6)), with a spectral strength given by

$$w_2 = A_S U, \quad (22)$$

where U is the wind speed (in m/s) at an elevation of 10 m. With this $W(Q_h)$ model, for a given wind speed there are two free parameters with which to fit data curves, γ_2 and A_S , γ_2 driving the frequency dependence, and γ_2 and A_S the level. Typical open-ocean values of these parameters are: $\gamma_2 \in (3.4, 4)$ and $A_S \in (5 \times 10^{-5}, 20 \times 10^{-5})$ m³-s. (More general forms of Eq. (6) are under consideration and will be incorporated into future σ_{int}^{surf} models.)

Thus, for this model, σ_{int}^{surf} depends on four environmental parameters: c_0 , U , A_S , and γ_2 . Note, with this model, σ_{int}^{surf} depends on frequency only through its dependence on γ_2 , and depends on the bistatic angle only through its dependence on $|Q_h|$.

4. BOTTOM INTERFACE SCATTERING

Our 3D bottom-interface scattering model σ_{int}^{bot} was described in the previous section. Here, after a discussion of its environmental inputs, we briefly explore some of its implications.

Geophysical Parameter Values

Table 2 lists some representative model parameter values for a range of bottom types: mud (silty clay), (coarse) sand, mudstone, limestone, and (rough) basalt. (These values derive from a number of sources. The parameters for mud, sand, and basalt derive from Essen [23] and Jackson [24]; those for limestone derive from Hamilton [25,26] and Jackson [24]; while those for mudstone derive from Fulford [27] and Kunz and Gauss [28].)

Table 2 — Representative Bottom-Interface Seafloor Parameters

	ρ_{bot}	c_p / c_0	c_s / c_0	γ_2	w_2 (m ⁴)
Mud	1.4	0.99-0.002i	0.1-0.004i	3.3	0.000518
Sand	2.0	1.2-0.005i	0.3-0.07i	3.3	0.006957
Mudstone	2.2	1.5-0.001i	0.5-0.0005i	3.5	0.0024
Limestone	2.4	2.7-0.004i	1.5-0.003i	3.3	0.004
Basalt	2.7	3.4-0.006i	1.8-0.006i	3.3	0.01862

Table 2 illustrates some typical parameter value trends, such that as the hardness of the bottom material increases, the density and sound speeds increase. Another observation is that the shear speed is often much less than the compressional speed. Indeed, the ratio of shear speed to compressional speed is constrained as follows [25]:

$$\frac{\text{Re}\{c_s\}}{\text{Re}\{c_p\}} \leq \sqrt{\frac{1-2\psi}{2-2\psi}}, \quad (23)$$

where ψ is Poisson's ratio. Typically [25], ψ ranges between 0.2 (hard materials) and 0.5 (soft materials— $\psi = 0.5$ for water), so that the corresponding range for this ratio is between 0.6 and 0. As regards bottom roughness, unfortunately (in contrast to the sea surface) few measurements exist. In view of this incomplete knowledge, it is typically²⁴ assumed that $\gamma_2 \sim 3.3$, and w_2 generally increases with material hardness. In practice, when in situ acoustic data are available, these latter two parameters are often estimated empirically via geoaoustic inversion (e.g., see Ref. 29.)

For the model illustrations in this paper, the imaginary parts of the sound speeds (which induce attenuation) will be assumed to be independent of frequency. Since our computations of σ_{int}^{bot} depend on the acoustic wavenumbers (Eq. (16)) (not explicitly on the sound speeds), this implies that the compressional- and shear-speed attenuations will increase linearly with frequency [26]. (It should be noted that although this is a standard assumption, there is evidence in the literature to the contrary, especially for water-saturated sediments [30-31]. This could have a significant impact on sediment acoustics, especially at mid-frequencies [32].) Conversion from attenuation's description as the imaginary part of the wave velocities $\text{Im}\{c_j\}$, where $j = p, s$, to the more commonly defined bottom sound absorption coefficient $\alpha_j = \kappa_j f_{(\text{kHz})}$ is provided by [8]

$$\kappa_j = -\frac{40000\pi}{\ln(10)} \cdot \frac{\text{Im}\{c_j\}}{[\text{Re}\{c_j\}]^2}. \quad (24)$$

If α_j is in its standard units of dB/m and the sound speeds in m/s, then the acoustic frequency must be in kHz (hence, the subscript). (For example, for the sand of Table 2, as $c_p = (1.2 - 0.005i)c_0$, we have $\kappa_p = 189.5/c_0$, or 0.125 dB/m/kHz for $c_0 = 1515$ m/s.)

Model Illustrations

We now illustrate the model by using parameters covering a range of environments, frequencies, and geometries. (For all modeling runs, we assumed $c_0 = 1515$ m/s and, except for Figs. 4(e) and 4(f), $\phi_{bi} = 180^\circ$.) While a comprehensive parameter study is beyond the scope of this paper, examples are provided to illustrate both how bottom-interface scattering strength depends on these quantities and how complex the scattering response can be. This, in turn, argues for the use of physics-based models (in lieu of an empirical model, such as that of Ellis and Crowe [33]) as bottom scattering strength submodels to active performance models, such as that of Fromm et al. [34], for predicting bistatic reverberation.

Model-Model Comparisons

Figure 2 illustrates some key points regarding the use of both SSA and standard first-order perturbation theory (PT) models. In this figure, monostatic predictions of backscattering strength at 3 kHz are plotted as a function of grazing angle. For the mud case, we see that all three predictions (SSA, PT for a fluid-solid interface, and PT for a fluid-fluid interface) lie atop one another (except near specular). However, as we progress to harder materials, elastic effects become increasingly important below the interface critical angles ($\theta_{cr}^j = \cos^{-1}(c_0 / \text{Re}\{c_j\})$ when $c_0 / \text{Re}\{c_j\} < 1$, for $j = p, s$). (Recall, $\text{Re}\{c_s\} \leq 0.6 \cdot \text{Re}\{c_p\}$ so that $\theta_{cr}^s < \theta_{cr}^p$ (for $\theta_{scat} \leq 90^\circ$) when both exist.) In these examples, for the sand and mudstone cases, fluid-fluid PT generally overpredicts the backscattering strengths below the compressional-speed critical angles ($\sim 33.5^\circ$ and 49° , respectively), while for both the basalt and limestone cases, fluid-fluid PT generally underpredicts the backscattering strength at low angles (below $\sim 40^\circ$). In contrast, the SSA and fluid-solid PT predictions are relatively close below the compressional-speed critical angles in all cases except for basalt, where there is only agreement below $\sim 40^\circ$. These examples argue that an elastic model is needed to accurately predict the acoustics at low scattering angles.

The basalt, limestone, and mudstone cases also illustrate the role that elastic effects can play in complicating the scattering response in the vicinity of and above the critical angles. For example, in the limestone case of Fig. 2(b), the local peak at 49° and null at 68° correspond to the shear and compressional critical angles,

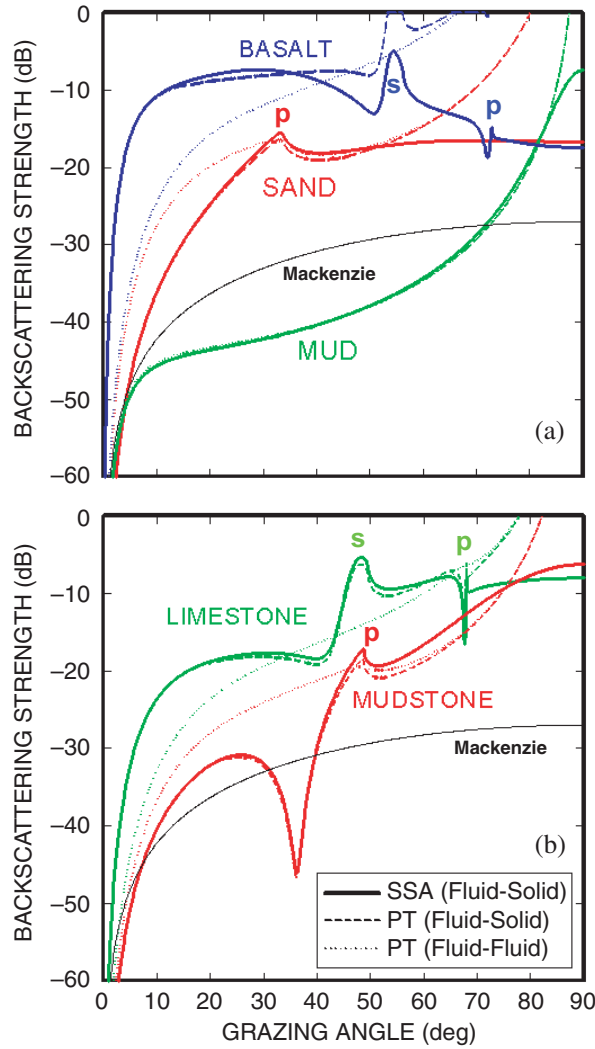


Fig. 2 — Monostatic model comparisons of the grazing-angle dependence of backscattering strength at 3 kHz using the values in Table 2. Included are the SSA and PT predictions for (a) mud, sand, and basalt, and (b) mudstone and limestone. For reference, a curve corresponding to the Mackenzie rule is included in each plot. The p's and s's identify the compressional- and shear-speed critical angles, respectively.

respectively. Furthermore, when the shear speed is significant, substantial subcritical-angle nulls can develop. This can occur even when $\text{Re}\{c_s\}$ is significantly less than c_0 as demonstrated with the mudstone case, where the shear speed is half the water sound speed. This example reinforces the importance of using an elastic model.

Another feature of the SSA is that its predictions behave well at all scattering angles, whereas PT begins to have problems near the specular direction (typically overpredicting the scattering strength) (Fig. 2). Also, note that the peak scattering response is not always at specular. Although not illustrated, rough-surface scattering strength can be quite sensitive to the value of the spectral exponent γ_2 [18], so that even for moderate grazing angles, the SSA is required to capture the physics.

Figure 2 highlights the advantage of using the best physics-based models available, as distinguished from the Navy-standard, phenomenological approaches (i.e., a $10 \cdot \log_{10} (\mu \sin^\alpha \theta_{inc} \sin^\alpha \theta_{scat})$ dependence for $\alpha = 0.5$ or 1, where μ is determined empirically). To illustrate this, the Mackenzie curve ($-27 + 10 \cdot \log_{10} \sin^2 \theta$ dB) has been included in Fig. 2 to allow comparison to the SSA model predictions. It is seen that, even translating the curves vertically, any agreements between the SSA and one-parameter empirical predictions are usually limited to a small set of angles. Hence, if acoustic data were just available at intermediate angles (say, 15-30°) and fit with an empirical curve, then one would typically overestimate the backscattering contributions at low, “long-range” grazing angles (e.g., 5°). Another general danger of the phenomenological approach in extrapolating data values to lower (or higher) angles is that the scattering mechanism can change (e.g., sediment-volume scattering above the compressional critical angle, and interface scattering below).

Model Predictions for Five Bottom Types

Figure 2(a) shows the wide range of backscattering values (30 dB or more at a given angle) that can be encountered in the ocean. Moreover, this variance depends strongly on the grazing angle (and frequency). In this example at 3 kHz, Fig. 2(a) shows that at 5° the acoustic response from basalt is about 35 dB stronger than that from mud or sand; at 20° the acoustic response from basalt is about 15 dB stronger than that from sand, which in turn is 20 dB stronger than that from mud; while at 80° the acoustic responses are roughly equal. Although these predictions are for 3 kHz, the general implications hold for a wide range of frequencies—e.g., model predictions at 300 Hz qualitatively look very similar to those of Fig. 2, so that, except toward specular, the relative backscatter strengths for the five materials described by Table 2 are generally maintained over 10 to 10000 Hz. This is illustrated in Fig. 3, which shows the frequency dependence of their backscattering strengths as predicted by the SSA at three grazing angles. This figure suggests that interface scattering strength generally has a monotonic frequency dependence, with levels typically increasing moderately with increasing frequency (the rate depending on the value of γ_2). An exception to this rule of the thumb occurs at high angles, where the scattering strength can flatten and even begin decreasing as the frequency increases.

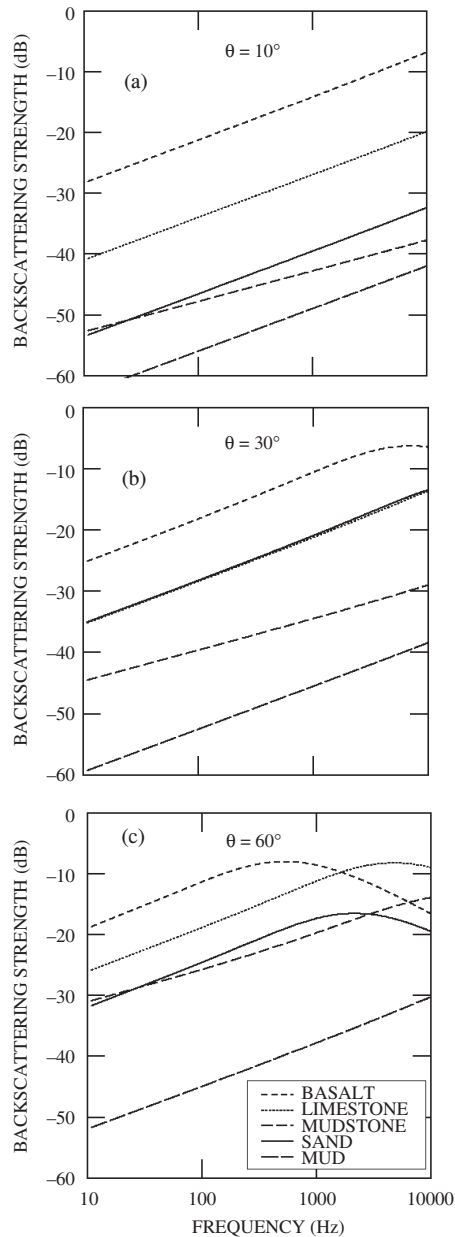


Fig. 3 — Monostatic predictions of the frequency dependence of backscattering strength at three grazing angles for mud, sand, mudstone, limestone, and basalt using the geophysical values in Table 2.

Bistatically, similar trends to those discussed above emerge. This is illustrated in Fig. 4, where the dependence of scattering strength on the scattered grazing angle θ_{scat} is highlighted. Figure 4(a) presents a bistatic version of Fig. 2(a) for an incident grazing angle θ_{inc} of 10° , suggesting that the general trends in scattering strength both between models and bottom types are preserved. (Also note that, bistatically the critical angles occur at θ_{cr}^j and $180^\circ - \theta_{cr}^j$, where $j = p, s$.)

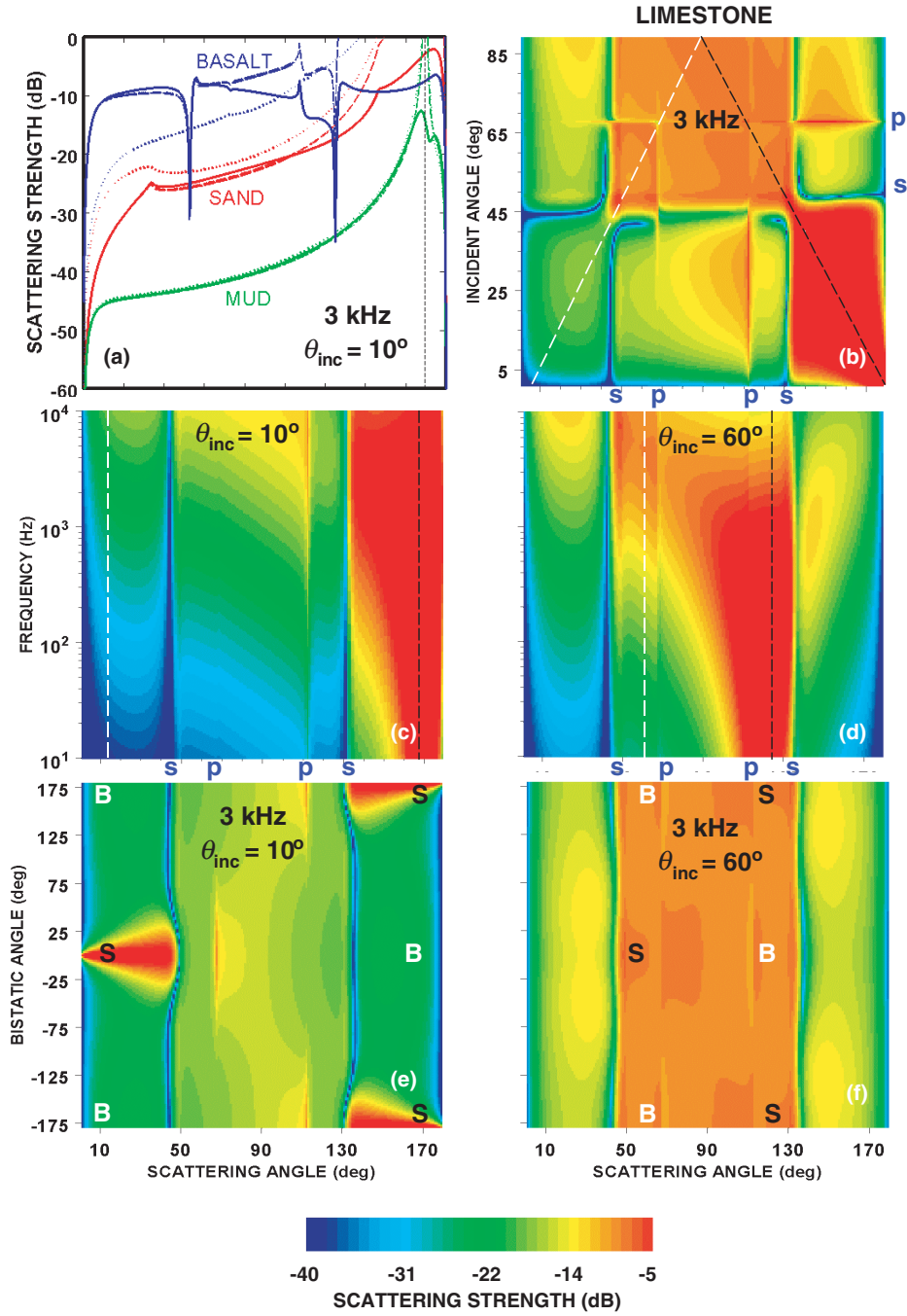


Fig. 4 — Bistatic scattering strength predictions for (a) mud, sand, and basalt, and (b)-(f) limestone, as a function of θ_{scat} using the geophysical values in Table 2. (The legend of Fig. 2 applies to (a).) The black dashed lines in (a)-(d) and the S's in (e)-(f) indicate the specular direction in each case, while the white lines in (b)-(d) and the B's in (e)-(f) indicate the backscatter directions. The p's and s's in the margins of (b)-(f) indicate the compressional- and shear-speed critical angles, respectively.

To explore this assertion more systematically, Figs. 4(b) through 4(f) display SSA predictions of scattering strength as a function of frequency and the three scattering angles for a single bottom type (the limestone of Table 2). Figure 4(b) shows scattering strength at 3 kHz as a function of both the incident and scattered grazing angles. The critical-angle effects are readily apparent, in this case when θ_{inc} or $\theta_{scat} = \sim 50^\circ$ or $\sim 130^\circ$ (shear-speed critical angles), and when θ_{inc} or $\theta_{scat} = \sim 68^\circ$ or $\sim 112^\circ$ (compressional-speed critical angles). As expected, we see that the scattering response is strong near specular. (We also see the requisite symmetry about $\theta_{inc} = \theta_{scat}$ for $\theta_{scat} \leq 90^\circ$ and about $\theta_{inc} = 180^\circ - \theta_{scat}$ for $90^\circ < \theta_{scat} < 180^\circ$.)

Figures 4(c) and 4(d) examine the scattering response at two incident grazing angles as a function of frequency and the scattered grazing angle. We see that for a fixed value of θ_{scat} , the scattering strength generally increases with increasing frequency at low scattering angles, but not always at high scattering angles. Figures 4(e) and 4(f) examine the scattering response at 3 kHz for the same two incident grazing angles as a function of the bistatic and scattered grazing angles. Not unexpectedly given our isotropic roughness assumption, away from the vicinities of the specular direction and the critical angles, the dependence on bistatic angle is relatively mild. (We also see the requisite symmetry about $\phi_{bi} = 0^\circ$, and that $SS(\theta_{inc}, \theta_{scat}, \phi_{bi}) = SS(\theta_{inc}, 180^\circ - \theta_{scat}, \phi_{bi} \pm 180^\circ)$.)

Figure 4 demonstrates that bottom scattering is a complex process requiring physics-based models to properly estimate its acoustic response.

Environmental Parameter Dependencies

Figures 5 and 6 present a study of the sensitivity of scattering strength to geophysical parameter values as functions of grazing angle and frequency, respectively. The goal is not to provide a complete depiction of how σ_{int}^{bot} depends on its inputs, but rather to gain a feel for the relative angle- and frequency-sensitivity of σ_{int}^{bot} to geophysical parameters. The scheme adopted for this purpose was to use the sand parameters of Table 2 as the default, and then independently vary the seven geophysical parameters over a wide range of realistic values. For simplicity, the study was restricted to monostatic SSA predictions at 1500 Hz.

Figure 5 reveals both how interesting the grazing-angle behavior of σ_{int}^{bot} can be, and its sensitivity to its input geophysical parameter values. It is apparent that across most of the figures, scattering strength generally increases as the grazing angle increases. Exceptions to this trend are regularly seen in the vicinities of the critical angles. For example, Fig. 5(a) shows a two-peaked ridge of maximum values, running from the vicinity of the critical angle at high w_2 values to specular at low w_2 values. Figure 5(b) shows that, for a given grazing angle, scattering strength has a fairly flat response as a function of compressional speed, above the ridge tracking the compressional-speed critical angle (the value of which increases as the compressional speed increases). Below this ridge, this situation is different: for a given compressional speed, the scattering strength has a mild monostatically-increasing response as a function of grazing angle.

Figures 5(c) and 5(d) reveal grazing angle valleys for particular combinations of shear speed and grazing angle values. To provide a more complete picture of the role of shear in influencing the acoustics, the default compressional speed of 1818 m/s has been increased to 4500 m/s in Fig. 5(d). In this case, a shear-speed critical angle exists when $\text{Re}\{c_s\} > c_0$ (as mapped out by the white line). As a result, a second valley tracking the shear-speed critical angle has emerged. As illustrated earlier with the mudstone case (Fig. 2(b)), these shear-induced nulls are significant manifestations of an elastic theory that needs to be accounted for when modeling reverberation in rocky environments (see, e.g., Ref. 28). Whether appreciable nulls manifest themselves for a given bottom at a given frequency will depend on the bottom's geophysical values. For example, in our artificial bottom of Fig. 5(d), if the shear speed were 1800 m/s, there would be a significantly weaker backscattering response at low grazing angles than if the shear speed were 2300 m/s.

For a given grazing angle, Figs. 5(e), 5(g), and 5(h) suggest a relatively mild dependence of scattering strength on the roughness spectral exponent and the attenuation values, while Fig. 5(f) shows the expected increase in scattering strength as the density ratio increases. Note in these four cases, local maxima in the vicinity of the compressional critical angle, and that, except for the density ratio, these maxima are typically strongest for low parameter values, with these maxima getting “smoothed out” for sufficiently high parameter values. For more elastic bottoms, a stronger dependence on γ_2 would be observed [18].

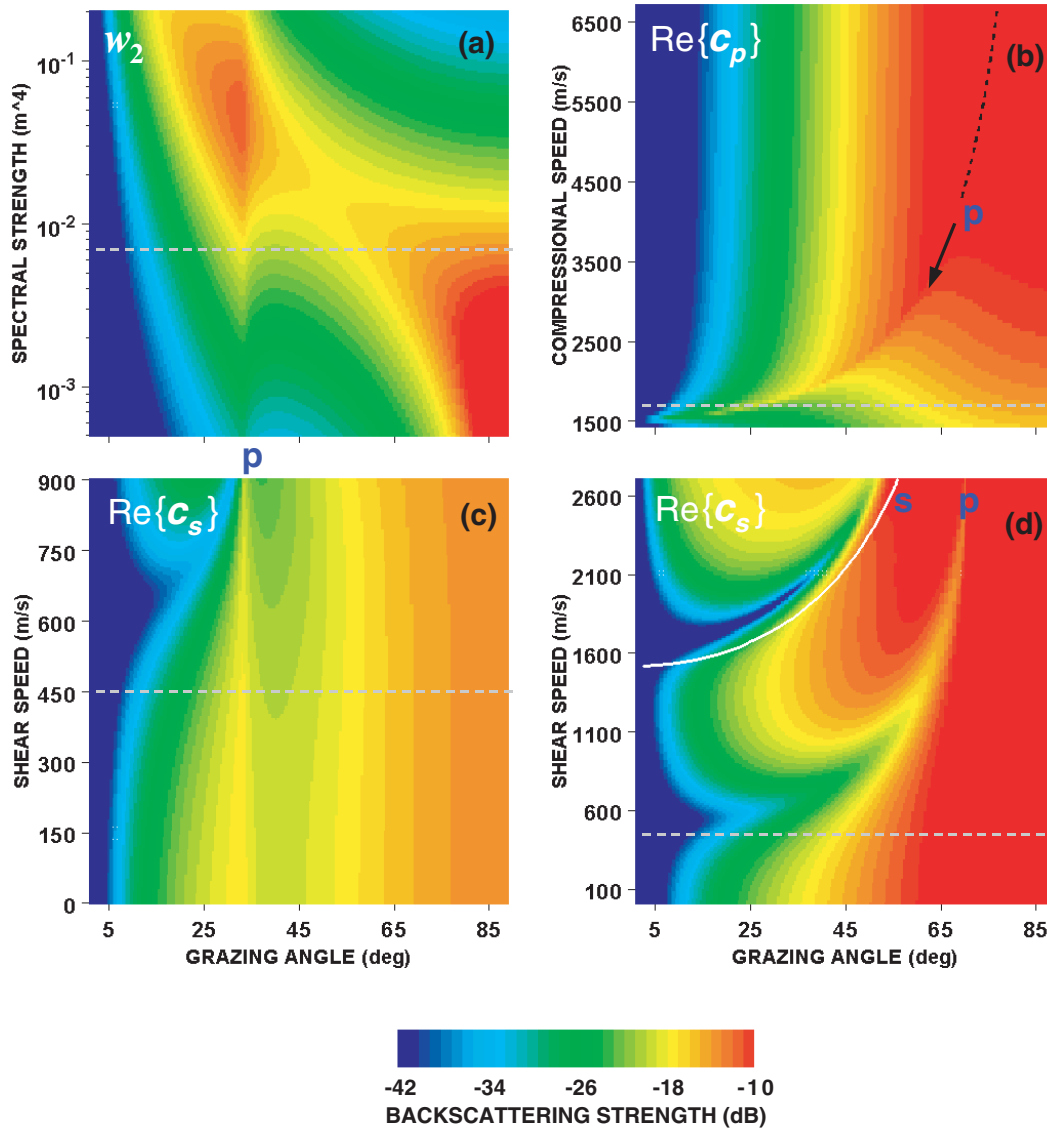


Fig. 5 — Monostatic predictions at 1500 Hz of the grazing angle dependence of bottom backscattering strength on geophysical parameter values. Using the sand parameters of Table 2 as the default, the displayed geophysical parameters were independently varied over the ranges shown. In (d), the default value of $\text{Re}\{c_p\}$ was reset to 4500 m/s, before varying the shear speed. The p's and the black curve/arrow in (b) indicate the compressional-speed critical angles in each case, while the s and the white curve in (d) indicate the shear-speed critical angles. The gray, dashed horizontal lines demark the default parameter values.

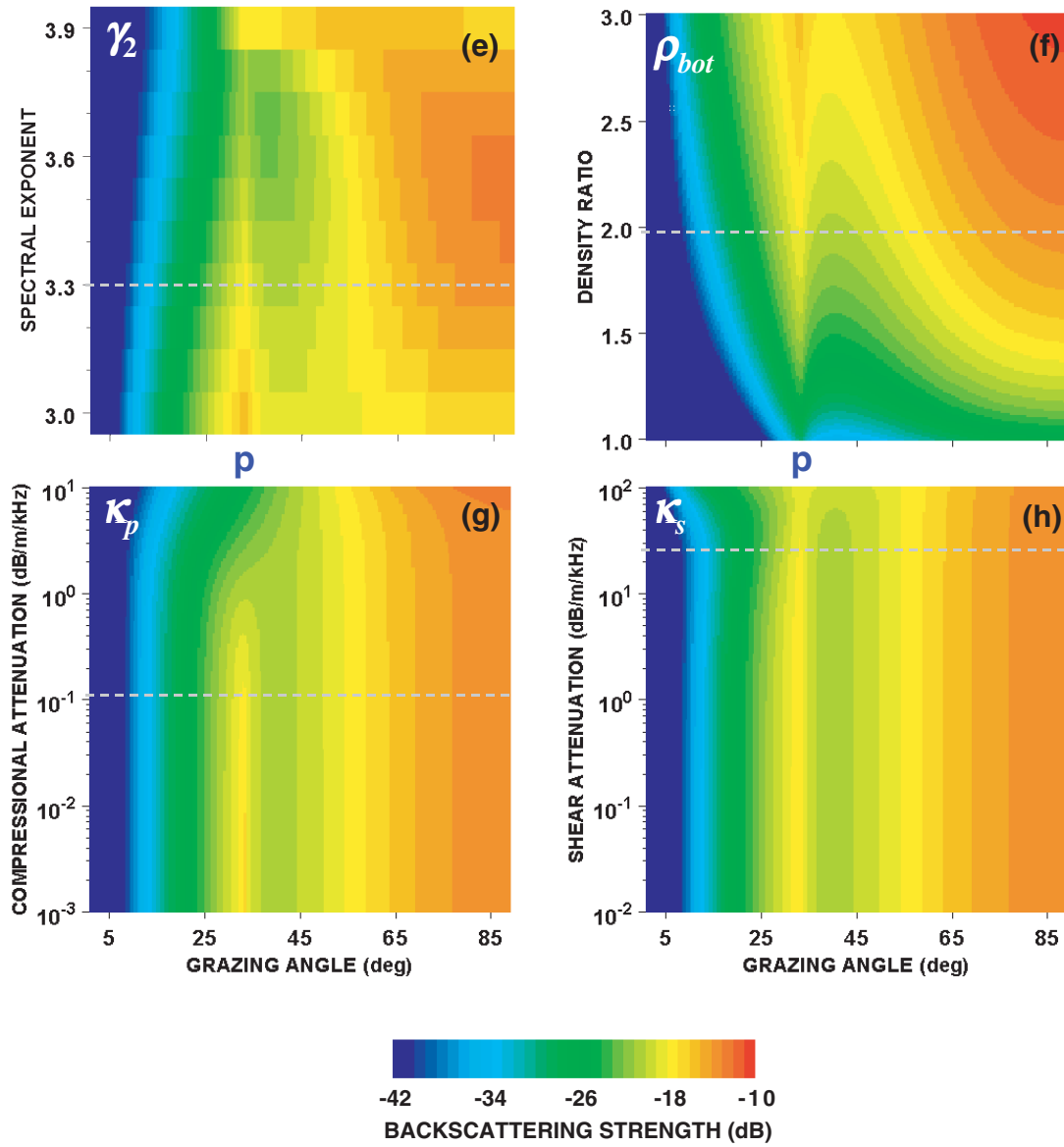


Fig. 5 (continued) — Monostatic predictions at 1500 Hz of the grazing angle dependence of bottom backscattering strength on geophysical parameter values. Using the sand parameters of Table 2 as the default, the displayed geophysical parameters were independently varied over the ranges shown. The p 's indicate the compressional-speed critical angle in each case. The gray, dashed horizontal lines demark the default parameter values.

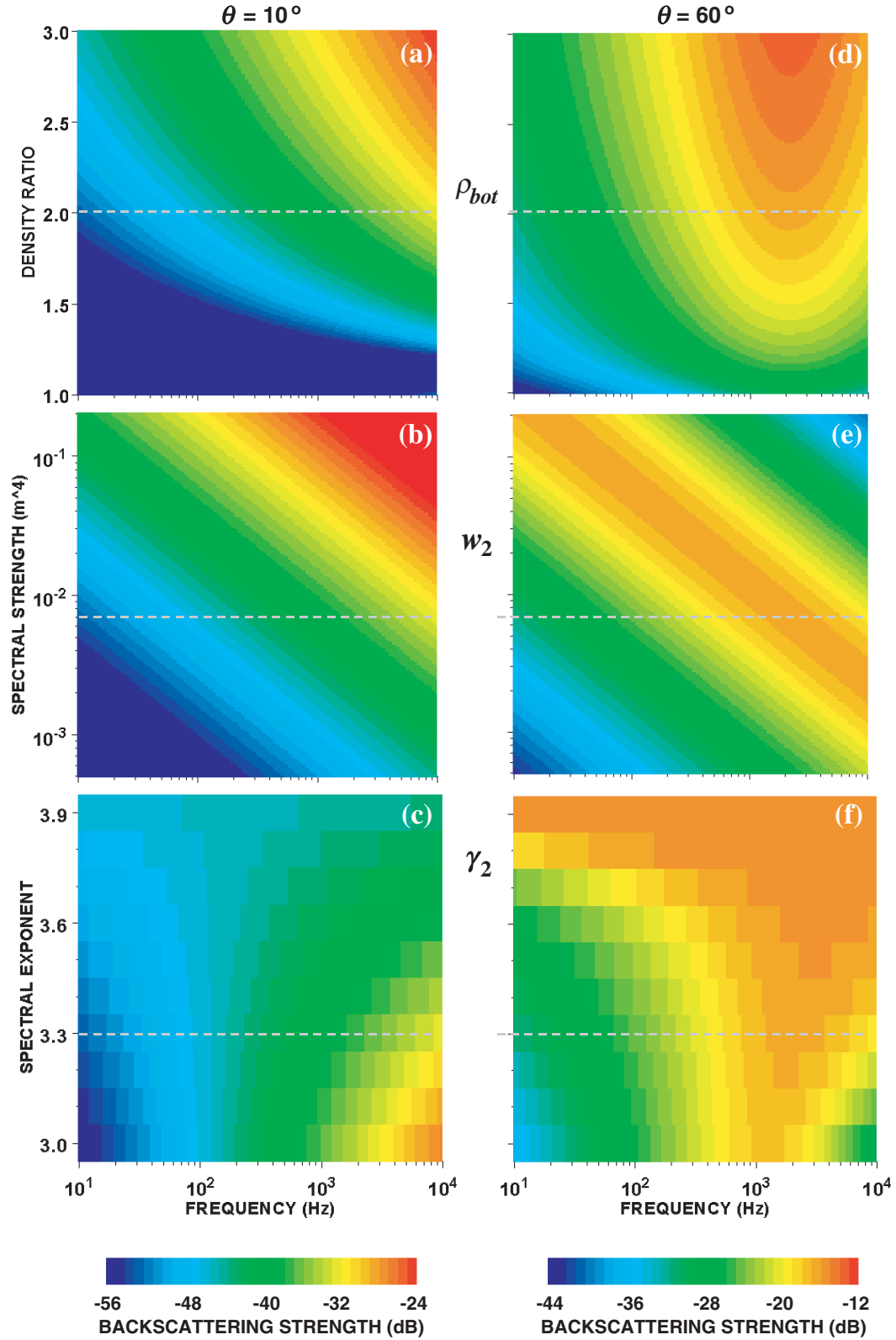


Fig. 6 — Monostatic predictions of the frequency dependence of bottom backscattering strength on three geophysical parameter values at two grazing angles. Using the sand parameters of Table 2 as the default, the displayed geophysical parameters were independently varied over the ranges shown. The gray, dashed horizontal lines demark the default parameter values.

Figure 6 shows some representative trends in the frequency behavior of bottom interface scattering strengths (cf., Fig. 3). Most geophysical parameters influence σ_{int}^{bot} in the manner of the density ratio, namely, a monotonically increasing dependence on frequency for a fixed value of the parameter at low-to-moderate grazing angles, with a more complex behavior at higher angles, for example, the ridges of maximum scattering strengths at 60° seen in Figs. 6(e) and 6(f). Figures 6(c) and 6(f) display the expected weaker frequency dependence as the value of the spectral exponent gets closer to 4.

Although not intended to be a comprehensive look at the dependence of σ_{int}^{bot} on its input parameters, this parameter study does suggest that, outside of the vicinity of the critical angles, the spectral parameters, sound speeds and density will generally have the most influence on the acoustics at low grazing angles (at least for $\gamma_2 \in [3, 4]$). Hence, obtaining good estimates for their values will be especially important.

Model-Data Comparison

Figure 7 shows an example data-model comparison of σ_{int}^{bot} for a rocky bottom. The monostatic data were collected over an exposed limestone bottom off the Carolina coast during the LWAD Focused Technology Experiment (FTE) 96-2 [35-36]. In this case, below the compressional critical angle, the model matched the observed grazing angle dependence, obtaining an rms data/model mismatch of 1.3 dB over backscatter angles of 15 to 70° for four frequencies across the 2.0 to 3.5 kHz band [36]. The unknown bottom parameters were estimated using simulated annealing: $\rho_{bot} = 2.6$, $c_p = (3.2 - 0.12i)c_0$, $c_s = (1.5 - 0.48i)c_0$, $w_2 = 0.0004 \text{ m}^4$, and $\gamma_2 = 2.6$. (In this case, $c_0 = 1487 \text{ m/s}$.)

This example illustrates how the model can be used to invert for hard-to-measure roughness spectral parameters, in particular for γ_2 : since it is the only environmental parameter that has any impact on the frequency dependence, broadband measurements can be used to estimate it. (Note, this assumes that the complex sound speeds can be taken to be effectively independent of frequency over the measurement band.)

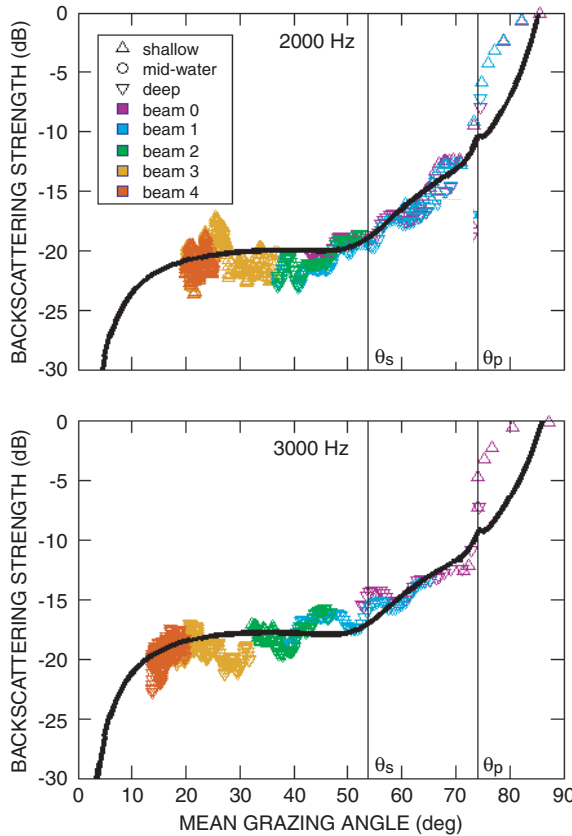


Fig. 7 — Data-model comparison for an exposed limestone bottom off the South Carolina coast. The shallow-water acoustic data (symbols) were collected monostatically using an omnidirectional source and a vertical-line array receiver during LWAD FTE 96-2 at Site Q (from Ref. 36).

In comparing these curves with the limestone curve in Fig. 2(b), note how in these LWAD 96-2 model predictions, the increased attenuation values have smoothed out the local peaks and nulls associated with the critical angles. Note also the model underestimates the data above the compressional critical angle, where volume-scattering contributions are expected.

Comments

While Figs. 2 through 7 have revealed complex relationships between σ_{int}^{bot} and its input parameters, these can be used to advantage in inverting for geophysical parameter values. By maximizing the frequency and grazing-angle (both incident and scattered if possible) coverage, systematic identification of these values can be pursued by exploiting distinctive acoustic signatures (such as critical-angle and shear-speed effects). Typically for a given ocean bottom, some values (such as the density ratio) are known with more confidence than others (such as the spectral strength). Hence, the use of a physics-based model such as the one presented here will allow an improved estimation of these other values, some of which can be difficult to measure even with the most sophisticated equipment. Furthermore, if these geophysical parameters are estimated from a small band of angles at a few frequencies, use of such a model will allow extrapolation in frequency and scattering angles with a degree of confidence that is not possible with empirical (e.g., Lambert's law) approaches. A physics-based acoustic model can also provide confidence levels to its predictions based on the confidence levels associated with the knowledge of its environmental inputs.

The model presented describes scattering from the water-sediment interface (as well as from sediment-sediment and sediment-basement interfaces). Not described in this paper is a general model for sediment-volume scattering. For such models, the reader is referred to the work of Jackson [8,16,37-40]. Coupling such a model with the interface-scattering model presented here would provide a general description of bottom scattering, which in turn, could be used to identify under what conditions the dominant scattering mechanism is the interface or the sediment volume.

5. VOLUME SCATTERING

Because of their variety and dynamic nature, estimating the scattering contributions of fish is particularly challenging. When fish are well separated from the ocean surface or bottom, recognizable broadband acoustic signatures identifying their presence and strength have been observed [41-44]. However, when fish are in the vicinity of an ocean boundary, as is common in the littoral, these characteristic fish signatures can undergo significant modification due to boundary-interference effects [5,45-46].

We now describe physics-based volume-scattering models that handle these boundary-interference effects, and provide a new understanding of the relative significance of surface, fish, and bottom scattering as functions of frequency, scattering angle, and biological and environmental factors. These plane-wave models are based on an established model of Love [2]. We begin with a review of his target strength formula, and follow with the extensions applicable to dispersed bladdered fish near the ocean surface and ocean bottom.

Single Fish Swimbladder Model

At low to mid frequencies, the primary scattering mechanism of a fish is its swimbladder [2]. Here, we first describe some of its physical properties, and then describe its free-field acoustic scattering properties.

Swimbladder Properties

Swimbladders resemble prolate spheroids or cylinders with major-to-minor axis (length-to-diameter) ratios up to 10. However, near resonance, it has been shown that the acoustic response, whether assuming a spherical, spheroidal, or cylindrical air-bubble model, generally varies by at most 30% [47-48]. Accordingly, as a first approximation we consider a spherical swimbladder, and then introduce corrections to account for real fish.

The fundamental (monopole) resonance frequency f_R of a spherical swimbladder is given by [2]

$$f_R^2 = \frac{3\gamma_a P}{4\pi^2 r^2 \rho_{tissue}}, \quad (25)$$

where γ_a is the ratio of specific heats of air (≈ 1.4), P is the ambient pressure in Pa, r is the swimbladder radius, and ρ_{tissue} is the density of the surrounding tissue (typically [2] taken as 1050 kg/m^3).

As a next step, we need to be more realistic on the following points before the above expression will describe the acoustic response of oceanic fish: (a) P , of course, depends on the (fish) depth $z > 0$; (b) r does too, but in a species-specific way; (c) actual swimbladders are nonspherical, and this too is species-specific. We discuss these in turn.

(a) It is elementary that the ambient pressure has the linear dependence $P = A + Rz$, where A is the atmospheric pressure (nominally 1 atm, i.e., 101325 Pa), and R is the rate at which the hydrostatic pressure increases with depth (approximately $A/10$ per meter). Thus we have

$$P = 101325 \cdot \left(1 + \frac{z}{9.8066} \right). \quad (26)$$

(b) For an inanimate balloon, there would be a simple dependence of r on z : an isothermal descent would just compress the balloon according to Eq. (26) and Boyle's Law [$z \Rightarrow P \Rightarrow V \Rightarrow r$]. Fish, however, control compression of their swimbladders in a manner empirically described by [42]

$$\begin{aligned} r &= r_0 & z < z_{comp} \\ &= \left(\frac{9.8066 + z_{comp}}{9.8066 + z} \right)^{1/3} r_0 & z \geq z_{comp}, \end{aligned} \quad (27)$$

where r_0 is the swimbladder radius at the ocean surface and z_{comp} is the depth where compression sets in. Both of these parameters are species-dependent. (r is now the radius of the equivalent sphere of the same volume V .) While it may seem that we are relying too heavily on the concept of a spherical swimbladder, namely that we seem to be correcting the radius of a supposedly spherical swimbladder based on the behavior of actual fish, when they in fact have nonspherical swimbladders. However, Eq. (27) relates *any* linear measure r of a swimbladder to its surface value r_0 . The shape really need not be spherical. But, when it is not, Eq. (25) needs to be modified.

(c) With swimbladders modeled as prolate spheroids, the modification takes the form [47]

$$f_{R\epsilon} = \zeta f_R, \quad (28)$$

where Weston's (depth- and species-dependent) correction factor ζ is a function of the swimbladder's minor-to-major axis ratio ϵ (< 1) given by [2]

$$\zeta = \epsilon^{-1/3} \sqrt{2q / \ln \left(\frac{1+q}{1-q} \right)}, \quad (29)$$

with $q \equiv \sqrt{1 - \epsilon^2}$. Values of ϵ generally range between 0.1 and 0.5, which correspond to ζ values of 1.25 to ~ 1.0 . (ζ is monotonically decreasing over this range of ϵ .) Note that as $\epsilon \rightarrow 1$, we have $\zeta \rightarrow 1$, as expected.

In most fish, bladder length is constant, held rigid in the anterior-posterior direction and on its dorsal surface by connective tissue and the skeleton, while bladder girth is free to compress inward from the lateral and ventral surfaces that adjoin the pliant abdominal cavity. Hence, we assign fish a spheroid-shaped bladder of constant length (usually $L/3$, where L is the length of the fish). For those fish where the bladder compresses (or expands) during vertical movements, we determine its new girth using $a_{sph} = \sqrt{3V_{comp} / 4\pi b_{sph}}$, where b_{sph} and a_{sph} are the major and minor axis radii, respectively, and V_{comp} is the compressed volume calculated from the r in Eq. (27). The new major and minor axes are used in the calculation of the spheroid-shape correction (Eq. (29)), while the equivalent radius of a sphere of the same volume is used in determining the resonance frequency (Eq. (25)).

In summary, Eq. (28) can be used as the corrected form of the fundamental frequency (Eq. (25)), with Eq. (26) for the pressure, Eq. (27) for the radius, and Eq. (29) for the shape-correction factor. Note that f_{Re} depends primarily on the ambient pressure ($f_R^2 \propto P$) and the swimbladder radius (f_R^2 inversely $\propto r^2$) that, in turn, depend primarily on fish species, size, and depth.

Scattering Model

Our scattering model will be that of Love [2], which represents an individual swimbladder-bearing fish as an air-filled, viscous elastic spherical shell with Weston's correction. This allows the acoustic cross section $\hat{\sigma}_{bladder}$ (in m^2) in the backscattered direction for a single swimbladder at the acoustic frequency f to be written in the form [2]

$$\hat{\sigma}_{bladder} = \frac{r^2}{\frac{f_{Re}^2}{f^2 H^2} + \left(\frac{f_{Re}^2}{f^2} - 1 \right)^2}, \quad (30)$$

where H is a damping factor:

$$\frac{1}{H} = \frac{2\pi r f^2}{f_{Re} c_0} + \frac{\xi}{\pi r^2 f_{Re} \rho_{tissue}}, \quad (31)$$

where ξ is the viscosity of fish flesh in Pa-s, typically [2] taken to have a value of 50 Pa-s. (Love's model [2] includes an additional term in Eq. (25) that accounts for the effects of swimbladder wall tension on f_R and a thermal damping term in Eq. (31). However, he has shown [2] that these terms are not generally of significance, so they have been omitted here.)

The model implies that a bladdered fish's target strength will depend primarily on its size and depth. Figures 8 and 9(a) provide representative illustrations of how the free-field frequency target-strength response of a fish, in this case, the salmon, changes with size and depth, respectively. Figure 8 shows how the salmon resonance pattern varies as its length is reduced from 0.5 m to ~0.03 m. (Here, we use a further approximation that provides an estimate of salmon swimbladder size given its length.) We see that as fish size is reduced, its target strength decreases and its resonance peak broadens and shifts upward in frequency. Figure 9(a) shows the salmon's resonance frequency increasing with depth due to the ambient pressure on its swimbladder increasing with depth (Eqs. (25)-(26)). (Also note that at a depth of 10 m, there is a shift in the frequency response as the salmon's swimbladder begins compression (Eq. (27)), as for this species [42], we assumed $z_{comp} = 10$ m.)

Fig. 8 — Predicted frequency dependence of the target strength of a single, free-field salmon at a depth of 10 m as parameterized by swimbladder size at the surface ($\sim 4\%$ of salmon length) (ζ was taken to be 1.12 and z_{comp} to be 10 m)

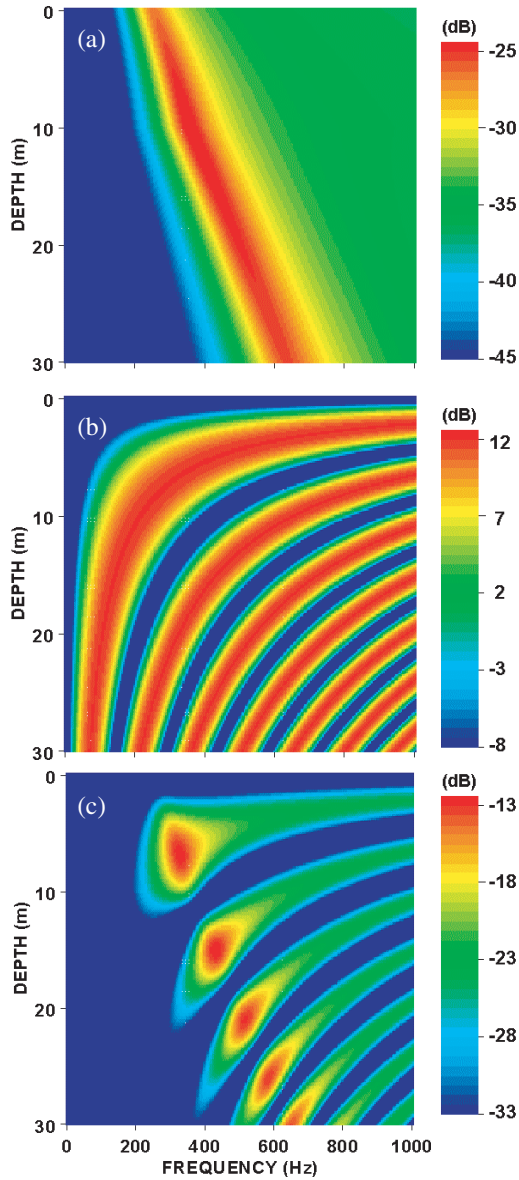
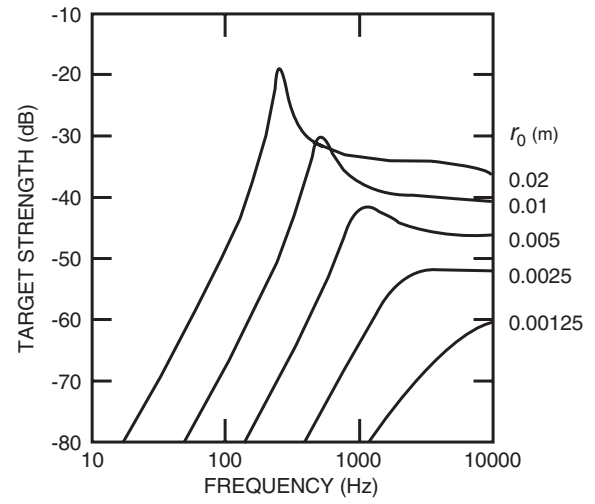


Fig. 9 — Predicted frequency and depth dependence of near-surface monostatic backscattering for a single salmon: (a) free-field target strength, and at a grazing angle of 10 deg, the (b) Lloyd's mirror interference pattern, and (c) near-surface scattering response. (z_{comp} , r_0 , and ζ were taken to be 10 m, 0.0144 m, and 1.12, respectively)

Layer of Fish Swimbladder Model

The total scattering from a layer of dispersed fish is simply the incoherent sum of scattering from the individuals. For the modeling in this paper, we make a further approximation by assuming a mean fish target strength $\bar{\sigma}_{bladder}$ at each depth (calculating a weighted average of a Gaussian distribution of N_r fish sizes):

$$\bar{\sigma}_{bladder} = \frac{1}{N_r} \sum_{i=1}^{N_r} w_i \hat{\sigma}_{bladder}(r_i), \quad (32)$$

where the w_i are normalized weights. (In practice, taking $N_r = 5$ is often sufficient.) Hence for a given species, the volume scattering strength of a layer of dispersed bladdered fish will depend primarily on their sizes, depths, and number densities (ρ_{fish}).

Fish Near Boundaries

Some fish species (such as salmon [42]) are typically close to the sea surface at night, and away from the surface during the day; some species are near the surface day and night (such as flying fish [49]); and some species are close to the bottom during the day, and away from the bottom at night (such as some species of rockfish [50]). When bladdered fish are near ocean boundaries, the scattering picture increases in complexity. Besides scattering from the rough interface itself, a fish scatters energy to a receiver along multiple paths (Fig. 10). The relative time delay of these four paths generates a pattern of constructive and destructive interference, the intensity of which depends strongly on the grazing angles, the distance of the scatterer from the boundary, the acoustic frequency, and for the ocean bottom, its physical properties. This can significantly alter the fish's scattered intensity (by a factor between 0 and 16).

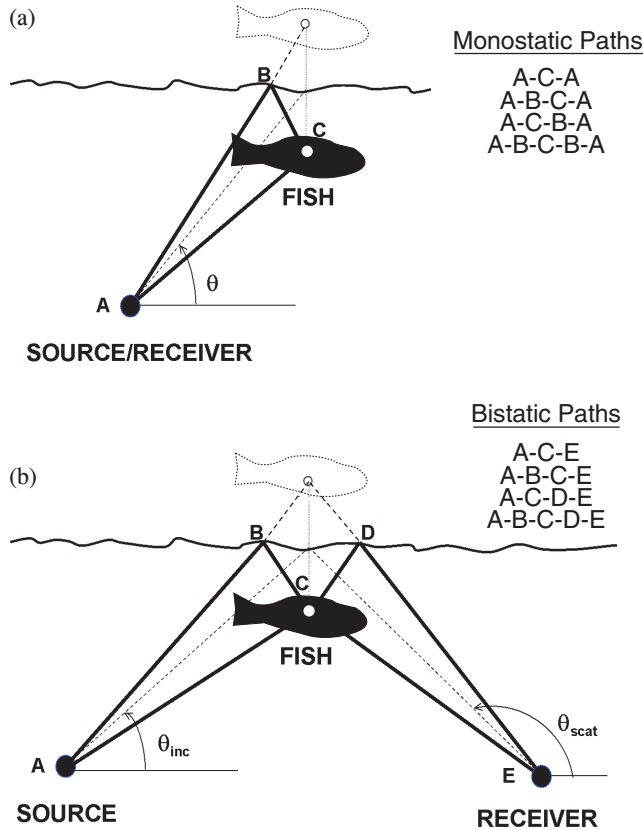


Fig. 10 — Primary near-boundary scattering paths, as illustrated for generic (a) monostatic and (b) bistatic surface geometries. (Monostatic paths A-B-C-A and A-C-B-A add coherently) (dashed fishes are image sources)

To model scattering from dispersed fish in the presence of such boundaries, we exploit the fact that the swimbladder typically occupies ~ 4 to 5% of a fish's volume [51], allowing us to model dispersed fish as point scatterers. Furthermore, our models assume the ocean boundaries are flat. (However, at our frequencies bias effects due to a rough surface can be shown not to be a significant problem.) Coupled with our point-scattering assumption, this implies that, to first order, the scattering cross sections of bladdered fish near a boundary depend on θ_{inc} and θ_{scat} , but not ϕ_{bi} . Finally, these models assume that the fish layer lies between the sonar and the boundary, and that the sonar is in the far field of the fish.

Fish Near the Ocean Surface

Because the density of air is so small, the air-sea interface basically reflects an incoming acoustic wave so that its phase is flipped. The images of sources and scatterers near the interface will also be 180° out of phase from the original. As a result, ensonification of a point scatterer at depth z in the vicinity of the sea surface (Fig. 10) creates an acoustic dipole, enhancing its backscatter cross section by $16 \sin^4(k_0 z \sin \theta)$ in the monostatic case [52]. Figure 9(b) provides a monostatic example of the resultant (Lloyd's mirror) interference pattern for a grazing angle of 10° .

To calculate the total scattered intensity due to a layer of bladdered fish near the sea surface, we need to convolve this Lloyd's mirror effect with the scattering due to the fish. Doing so for bistatic geometries yields for fish in layer(s) covering depths z_1 to z_2 ($z_2 > z_1$):

$$\sigma_{fish}^{surf} = 16 \int_{z_1}^{z_2} \rho_{fish}(z) \bar{\sigma}_{bladder}(f, z) \sin^2(k_0 z \sin \theta_{inc}) \sin^2(k_0 z \sin \theta_{scat}) dz. \quad (33)$$

Thus, for this model, σ_{fish}^{surf} for fish uniformly distributed (over a given layer) depends on eight environmental and biological parameters: c_0 , z_1 , z_2 , z_{comp} , ρ_{fish} , r_0 , ϵ , and N_r .

A look at Eq. (33) suggests that when $k_0 z \sin \theta$ is small, such as when the scatterer is within a few wavelengths of the surface, or the grazing angle is very low, then the Lloyd's mirror pattern can modify the free-field acoustic response by a factor between 0 and 16. Figure 9(c) shows a monostatic example of this modification at $\theta = 10^\circ$ for the single salmon of Fig. 9(a). (Note the enhanced scale of Fig. 9(c).) In this case, very near the surface the salmon resonance response is suppressed (minimum of the interference pattern). At deeper depths, the maxima of the Lloyd's mirror pattern are more closely spaced in frequency and depth, so that a layer of fish over, say, 20 to 30 m, ends up mimicking the free-field frequency response (at this grazing angle), albeit at enhanced levels.

Fish Near the Ocean Bottom

In contrast to the air-sea interface, which effectively repels acoustic energy, the water-sediment interface has some rigidity and attracts acoustic energy. As a result, whereas the case of a point scatterer near the sea surface leads to a relatively simple and compact formula, the general formulation for the ocean bottom will be more complicated. (In the presence of a non-pressure-release boundary, a point scatterer is not a dipole but is in general described by a series of higher-order moments.) As with the surface model, this bottom model has as its fish-scattering kernel the cross-section scattering formula of Love (Eqs. (25)-(32)). However, for the bottom, we assume a (flat) fluid/elastic-solid interface.

We first define the complex bottom-reflection coefficients [13]

$$R_j = \frac{a_j - 1}{a_j + 1}, \quad (34)$$

where the a_j are given by Eq. (17). Hence, σ_{fish}^{bot} will depend on ρ_{bot} , c_p , c_s , and c_0 , but not on w_2 or γ_2 .

With this definition, we can now write down our general bistatic scattering cross section formula for a layer of bladdered fish dispersed over depths z_1 to z_2 in a waveguide of depth D :

$$\sigma_{fish}^{bot} = \int_{z_1}^{z_2} \rho_{fish}(z) \bar{\sigma}_{bladder}(f, z) |1 + R_{inc} \exp[2ik_0(D-z)\sin\theta_{inc}]|^2 |1 + R_{scat} \exp[2ik_0(D-z)\sin\theta_{scat}]|^2 dz. \quad (35)$$

Thus, for this model, σ_{fish}^{bot} for fish uniformly distributed (over a given layer) depends on fourteen environmental and biological parameters: c_0 , z_1 , z_2 , z_{comp} , D , ρ_{fish} , r_0 , ϵ , N_r , $\text{Re}\{c_p\}$, $\text{Im}\{c_p\}$, $\text{Re}\{c_s\}$, $\text{Im}\{c_s\}$, and ρ_{bot} .

To gain some insight as to the effect of the ocean bottom on σ_{fish}^{bot} , consider the limiting case of a perfectly reflecting bottom (Neumann boundary conditions), where $R_j \rightarrow 1$. In this special case of an ideally hard, flat bottom, Eq. (35) reduces to the case of a double monopole:

$$\sigma_{fish}^{bot} = 16 \int_{z_1}^{z_2} \rho_{fish}(z) \bar{\sigma}_{bladder}(f, z) \cos^2[k_0(D-z)\sin\theta_{inc}] \cos^2[k_0(D-z)\sin\theta_{scat}] dz. \quad (36)$$

This formula suggests that the acoustic scattering response of a fish near the ocean bottom at low scattering angles is generally less variable than that of a fish near the sea surface ($\sim \cos^4$ vs $\sim \sin^4$ for the pure backscatter case). Furthermore, in contrast to the sea-surface case, a fish on the bottom is in a maximum of the interference pattern (source and its image are in phase). (For a realistic, nonideal bottom, this maximum will generally be slightly above the bottom.) Hence, fish resting on the bottom not only still can be appreciable scatterers, but potentially mistaken for bottom scatterers (e.g., surface features or sediment-volume heterogeneities).

Figure 11 is an ocean-bottom analog to Fig. 9. In this example, we are modeling the frequency and depth dependence of the monostatic backscattering response from a single salmon in 100 m of water at separations of 0 to 30 m from a sandy bottom (Table 2). Figure 11(a) displays the salmon's free-field target strength response, while Fig. 11(b) displays the interference pattern at a grazing angle of 10° . It is seen that in this case, a fish very near the bottom will generally be in a maximum of the interference pattern. We also see that, due to the salmon's higher resonance frequency at these depths, the free-field frequency response is more closely mimicked in this near-bottom case than in the near-surface case (Fig. 9(c)) (as these maxima are more closely spaced in depth at the higher frequencies). As with the surface case, an important boundary-interference effect is the significant enhancement of the free-field backscattering strengths. (Note the enhanced scale of Fig. 11(c).)

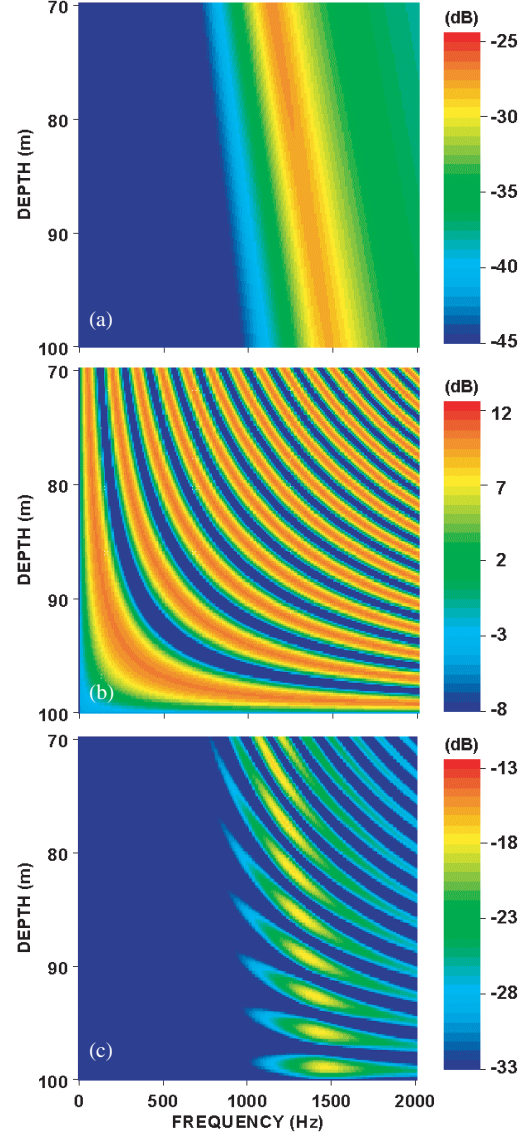
Comments

For practical applications of this model, for example, as kernels in reverberation or performance models, a field of discrete fish is treated as a spatially (and temporally) uniform layer, which in turn is treated as an effective modifier of boundary properties. Thus, they can be used like a surface or bottom scattering strength with no need to introduce a separate layer into the modeled waveguide.

Model Illustrations

We now illustrate the models with a few examples. Here, for simplicity, we assume layers of fish that are uniformly distributed in depth (and, locally, uniformly distributed in range). (For all examples, we take $\phi_{bi} = 180^\circ$.)

Fig. 11 — Predicted frequency and depth dependence of near-bottom monostatic backscattering for a single salmon above a sandy bottom in 100 m of water: (a) Free-field target strength, and at a grazing angle of 10 deg, the (b) interference pattern and (c) near-bottom scattering response. (z_{comp} , r_0 , and ζ were taken to be 10 m, 0.0144 m, and 1.12, respectively.)



Fish Near the Ocean Surface

The model for σ_{fish}^{surf} , when combined with a surface-scattering model, provides a prediction of scattering strength appropriate for the air-sea interaction zone (when the acoustic source and receiver are in the far field of the scatterers). The total scattering strength is the sum of contributions from the air-sea interface (σ_{int}^{surf}), fish (σ_{fish}^{surf}), and bubbles (σ_{bub}):

$$SS_{TOTAL}^{surf} = 10 \cdot \log_{10}(\sigma_{int}^{surf} + \sigma_{fish}^{surf} + \sigma_{bub}). \quad (37)$$

(A model for σ_{bub} will be described in the section on surface scattering. Here, we take $\sigma_{bub} \equiv 0$.)

In analyses of acoustic backscatter collected during various low-frequency (70 to 1500 Hz) CST surface-scatter measurements, the presence of fish has sometimes been inferred, particularly during periods of low sea states [45,53]. In these cases, for fish deeper than ~ 10 m, recognizable and robust broadband volume scattering signatures were typically seen at low grazing angles, such as a frequency resonance and a flatness in grazing angle. When fish are shallower, these acoustic signatures can undergo significant modification. For example, in

some of the lowest sea state cases from the CST Gulf of Alaska experiments (CST-4 and CST-7 Phase 2), measured low-grazing-angle scattering strengths were suggestive of air-water interface scattering, yet concurrently measured continuous wave (cw) spectra showed Gaussian spreads centered at zero frequency shift, consistent with fish or bubbles [45]. However, no significant inclusion of bubbles was observed (or, in general, expected for wind speeds less than 5 m/s) [54]. The model for σ_{fish}^{surf} just described helps resolve some of these mysteries and provides a new understanding of the relative significance of interface, fish, and bubble scattering as a function of frequency, scattering angle, and biological and environmental factors.

Figure 12 presents monostatic backscatter model predictions for salmon uniformly distributed over two sets of layer depths, corresponding to their typical nighttime (0.5 to 2 m) and daytime (15 to 40 m) depths during CST-7 Phase 2 [42]. (Typical Gulf of Alaska sizes and densities were assumed [42].) Figure 12(b) displays the frequency resonance and flat grazing angle response that occur when the salmon are a number of wavelengths away from the sea surface. Adding on the scattering contribution of the air-sea interface, Fig. 12(d) reproduces the aforementioned acoustic behavior observed in the CST Gulf of Alaska surface scatter measurements. In contrast, when the fish are very near the air-sea interface ($< \text{few wavelengths}$), both the characteristic flatness in grazing angle and any obvious resonance behavior within a given frequency band can disappear (Figs. 12(a) and 12(c)). This suggests an alternate explanation for the enhanced levels (relative to rough surface-scattering theory predictions) of low-frequency surface-scattering strengths that have been observed in low-to-moderate sea states. Bistatically, the scattering picture is similar for fish away from the surface (Fig. 12(f)), and more complicated for fish very near the surface (Fig. 12(e)), demonstrating the need for measuring fish behavior.

In general, when fish are near the air-sea interface, a rich variety of frequency and grazing-angle behaviors of σ_{fish}^{surf} can be observed. Figure 13 illustrates this with a real-world example of backscattering from near-surface salmon during a low-sea-state, night-time measurement in the Gulf of Alaska during the Active Adjunct to Undersea Surveillance (AAUS) Leg 5 Area 1 experiment (May 1984) [45]. These displays of σ_{TOTAL}^{surf} demonstrate that, in some cases, fish can be the dominant scattering mechanism at low grazing angles, even at low densities—average salmon densities in this environment are typically a few hundred individuals per square kilometer [42]. (In this case, with $\sigma_{fish}^{surf} > \sigma_{int}^{surf}$ by up to 20 dB at 10° .) It further illustrates the utility of the physics-based scattering model as an inversion tool. After inversion for the salmon's density and depths (in this case, 2.5 to 7 m), the model allows extrapolation in frequency and angle. In this case, the prediction is low backscatter levels at very low grazing angles ($< \sim 5^\circ$).

Fish Near the Ocean Bottom

It has just been demonstrated that, in some cases, backscatter from fish near the sea surface can dominate (and be confused with) surface backscatter from the air-water interface (and bubble clouds). Similarly, fish near the ocean bottom are potentially a competing scattering mechanism, both to the bottom interface and to the sediment volume. Analogous to the ocean-surface case, the total scattering strength will be modeled as the sum of contributions from the ocean-bottom interface (σ_{int}^{bot}), fish (σ_{fish}^{bot}), and the ocean-bottom volume (σ_{vol}^{bot}):

$$SS_{TOTAL}^{bot} = 10 \cdot \log_{10} \left(\sigma_{int}^{bot} + \sigma_{fish}^{bot} + \sigma_{vol}^{bot} \right). \quad (38)$$

(Here, we take $\sigma_{vol}^{bot} \equiv 0$.)

Figure 14 shows a low-frequency example of backscattering due to shoaling rockfish over a mudstone bottom. This instructive example derives from the modeling of low-grazing-angle bottom backscattering data collected by Kunz of NRL during LWAD 99-3 [28]. In this case, the acoustic data followed a $\mu \sin \theta$ angular dependence (Fig. 14(a)), an empirical relationship commonly ascribed to bottom backscattering. However, upon modeling the scattering contributions of both the rockfish and the bottom, it was found [28] that this dependence was really the coincidental combination of rockfish scattering at low angles and mudstone scattering at higher angles.

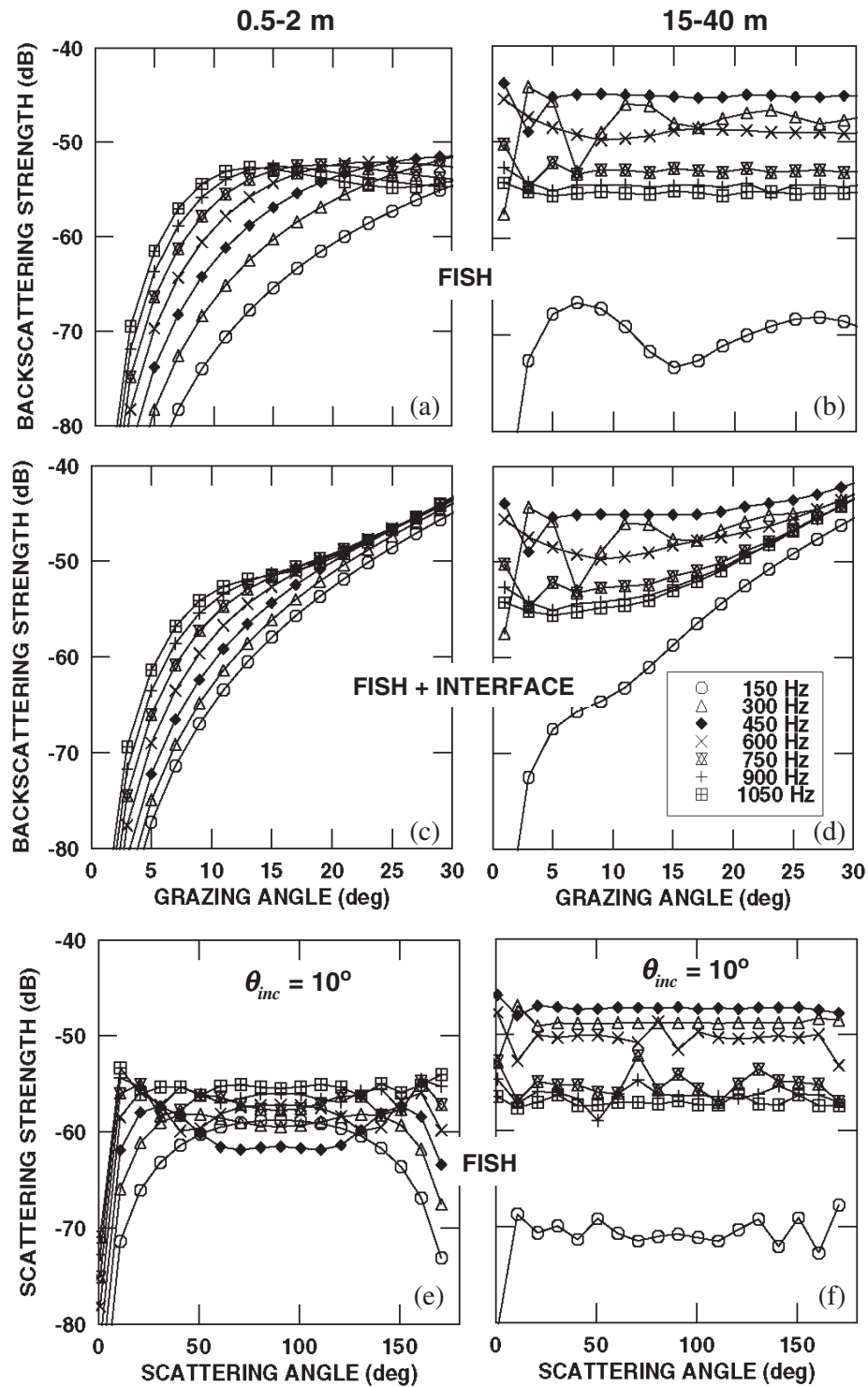


Fig. 12 — Monostatic (a)-(d) and bistatic (e)-(f) predictions of the angular dependence of the scattering strength of near-surface salmon (at typical Gulf of Alaska sizes and densities [42]) as a function of frequency (150 to 1050 Hz) for two sets of fish-layer depths. Subplots (c)-(d) respectively include the contribution of interface scattering (for a wind speed of 5 m/s) to the near-surface salmon scattering displayed in (a)-(b).

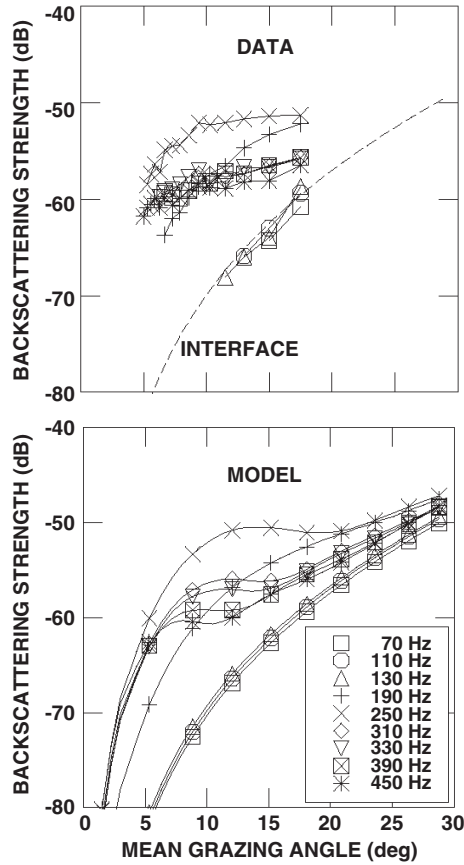


Fig. 13 — Data-model comparison for near-surface salmon + interface scattering in the Gulf of Alaska. The wind speed was 3.0 m/s. The acoustic data were collected quasi-monostatically using omnidirectional explosive charges as sources, which detonated at depths of ~ 457 m below a horizontal receiver towed at a depth of ~ 210 m. For reference, the top plot includes the predicted contribution of interface scattering at 110 Hz (dashed curve).

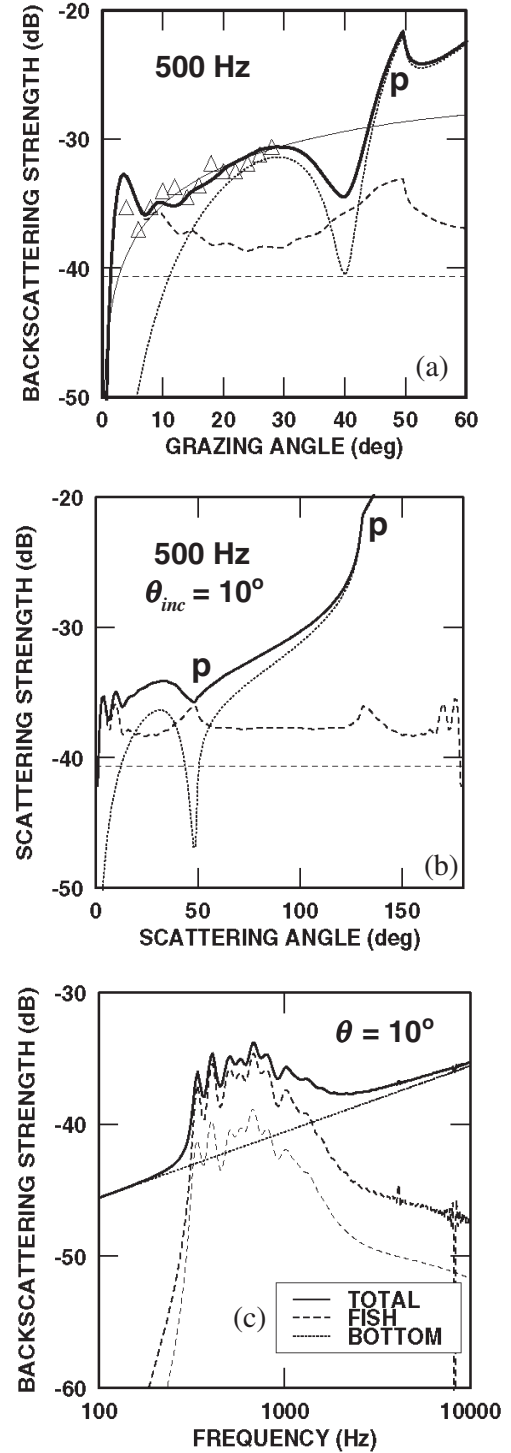


Fig. 14 — Predicted (a)-(b) angular and (c) frequency dependence of the scattering strength of rockfish uniformly distributed 0-15 m above a mudstone bottom in 91 m of water. Included in (a)-(c) as lightly dashed curves, are the free-field rockfish scattering responses (i.e., not including bottom-interference effects). Included in (a) are data (symbols) from LWAD 99-3, [28,46] and a thin solid curve representing $-27.5 + 10 \cdot \log_{10} \sin \theta$ dB. In (a)-(b), the p's indicate the compressional-speed critical angles.

To illustrate this sort of interplay more clearly, Fig. 14 presents a simplified version of the LWAD 99-3 scattering scenario. (Refs. 28 and 55 provide more details.) Here, we consider three varieties of rockfish (small, medium, and large) in 91 m of water that are uniformly distributed 0 to 15 m above the mudstone bottom parameterized in Table 2. (Here, $c_0 = 1485$ m/s.) The average rockfish layer density was assumed to be 0.06 fish/m² (i.e., $\rho_{fish} = 0.06 \text{ fish/m}^2 \div 15 \text{ m} = 0.004 \text{ fish/m}^3$). Figure 14(a) displays monostatic predictions of the backscattering strength at 500 Hz from the rockfish (thick dashed curve), the mudstone bottom (dotted curve), and their total (thick solid curve). A $\mu \sin \theta$ curve matched to the acoustic data (symbols) overlays these curves. In this case, we see that which mechanism dominates is a strong function of grazing angle and that, even at these relatively low densities, the rockfish dominate the scattering below 15°. At increasingly higher densities, rockfish scattering would dominate the scattering over an increasingly broader range of angles.

Bistatically, we see a similar picture. Figure 14(b) shows that the basically flat dependence of rockfish scattering strength with scattering angle implies their contribution at 500 Hz will be primarily at low scattering angles (and minimal near specular). Also apparent in Figs. 14(a) and 14(b) are local peaks in the rockfish's scattering response associated with the compressional-speed critical angle (e.g., at ~49°).

Another factor affecting the relative dominance of fish and bottom scattering mechanisms is frequency. Figures 14(a) and 14(b) presented predictions for 500 Hz that correspond to the peak acoustic response of the rockfish at these depths. Off resonance, a fish's target strength is reduced (Fig. 14(c)), so that which scattering mechanism dominates can depend on a complex mix of factors. This example reinforces the usefulness of physics-based scattering models for both isolating the contributions of different scattering mechanisms, and allowing extrapolation with confidence in frequency and angle (especially bistatically).

As demonstrated above, the acoustic response of fish can be mistaken for bottom scattering in some cases (especially if only narrow ranges of frequencies or angles are sampled). In particular, since fish generate characteristic broadband frequency responses, their scatter could be confused with sediment-volume scatter, also generally a broadband frequency-dependent phenomenon (a cautionary tale for those doing geo-acoustic inversions). Furthermore, for a nonuniform distribution of fish, say shoaling fish, the resultant spatial variability in σ_{fish}^{bot} could be mistakenly attributed to sediment-volume heterogeneities, and local “hot spots” of fish to “geo-clutter.” Figure 15 provides a data example from October 2000 of highly localized fish schools on the New Jersey continental shelf. These sonar images were generated by Turgut of NRL [56] using a downward-looking, 2 to 8 kHz chirp echo sounder, which pinged twice a second as it passed over the bottom at a rate of ~3 m/s. (In this case, the backscatter levels from the fish were within 10 dB of those from the sandy bottom.)

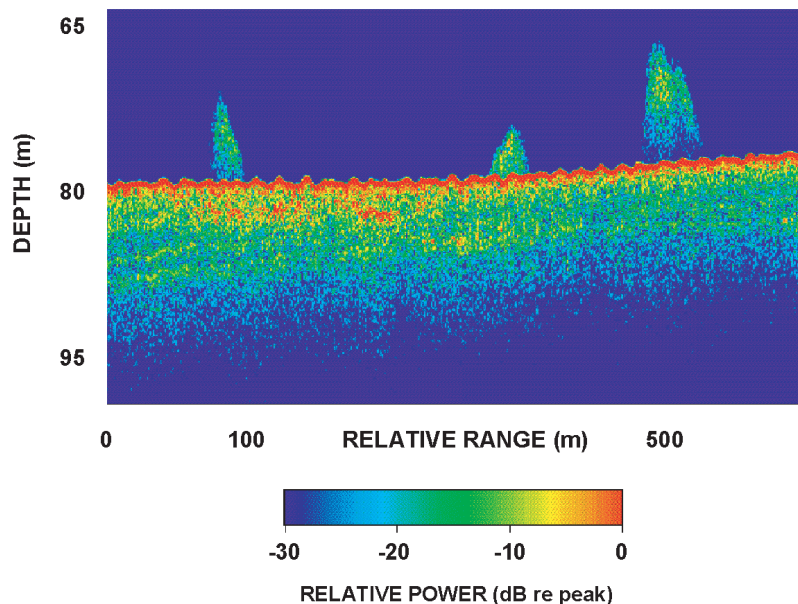


Fig. 15 — Daytime chirp sonar (2-8 kHz) record displaying fish schools adjacent to the ocean bottom on the New Jersey Shelf (~39°20'N, 72°50'W). The nominal water depth was 80 m (courtesy of A. Turgut, NRL [56])

Comments

For both boundaries, one consequence of these boundary-interference models is that they predict that a fish's target strength is generally enhanced. Typically, the effect is to increase the average scattered intensity by a factor of 4 (6 dB). (When θ_{inc} exactly equals θ_{scat} , this factor is 6 (~7.8 dB); however, as these two angles begin to differ, the factor quickly converges to a value of 4. Figure 14 provides examples of this enhancement—the differences of the thick and thin dashed curves.)

Fish near the ocean surface or bottom in shallow water often are in schools. Modeling and experiments [4,57] suggest that resonant coupling and multiple scattering from the schools can cause shifts in the amplitude and frequency of the swimbladder resonance. This could result, for example, in increases in scattering at frequencies somewhat below an individual fish's expected resonance. So, when fish school in the presence of a boundary, further modification to the above formulas will be required to accurately model their scattering response.

Because fish have characteristic frequency dependencies to their acoustic responses, broadband measurements combined with these models can help discern the extent to which the observed scattering is due to fish or to the ocean boundary. Also, day/night measurements illustrating fish behavior can help a great deal in this regard.

6. SURFACE SCATTERING

The scattering picture in the dynamic air-sea boundary zone is complex. When wave breaking is significant, scattering from the rough air-sea interface is augmented with scattering from subsurface bubbles. At high frequencies, resonant scattering from individual bubbles is known to be an important scattering mechanism [58]. At lower frequencies (<~5 kHz), however, observations on the temporal response of scattering can be used to rule out resonant scattering from being a significant scattering mechanism. In this case, acoustic scattering from bubbles can still occur through scattering from assemblages of bubbles within bubble clouds, or from entire clouds. This is primarily due to Bragg scattering from inhomogeneities in the sound-speed field, which is proportional to the Fourier transform of the index of refraction field. At these frequencies, the index of refraction depends on the air-void fraction, but not on the details of the bubble distribution. Hence, a key environmental descriptor of bubble clouds at these lower frequencies is the air-void fraction.

Recent low-frequency (< 1500 Hz) surface-scattering measurements under the CST program have demonstrated with high confidence that low-frequency scattering from bubble clouds of low air-void fraction (< 0.01 %) (microbubble clouds) is responsible for the high reverberation levels observed in high sea states [45,59]. In conjunction with the key acoustic measurements, Farmer and Vagle of the Institute of Ocean Sciences made measurements of the in situ air-void fraction that they have been able to relate empirically to the wind speed [54]. Spurred by these CST scattering and oceanographic measurements, NRL has developed a semi-empirical model for estimating the scattering strength due to bubble clouds that is parameterized solely by the wind speed.

This bubble-cloud scattering model has been integrated with our model for σ_{int}^{surf} into a broadband, fully bistatic surface scattering strength (SSS) model:

$$SSS = 10 \cdot \log_{10} \left(\sigma_{int}^{surf} + \sigma_{bub} \right). \quad (39)$$

The resulting model is parameterized by frequency (10 to 5000 Hz), the scattering angles (incident, scattered, bistatic), and environmental variables (wind speed and two surface-wave spectral parameters). (As will be discussed shortly, a further approximation allows SSS to be parameterized solely by wind speed.) A particular advantage of this physics-based model is its reliance on readily observable oceanographic variables [60-61], quantities that can be measured in near-real-time on regional scales using airborne [62] and spaceborne [63] remote sensing.

This model offers significant advances over previous (purely empirical, monostatic) algorithms [64-65], namely physics-based descriptions of scattering from both the rough air-sea interface and subsurface bubbles; fully bistatic calculations; and applicability to a broader range of frequencies.

In this section, after a brief summary of data sources used in deriving the semi-empirical fits, the previously presented σ_{int}^{surf} model is illustrated and then further refined. This is followed by a description of our bistatic model for σ_{bub} . These models are then used to briefly explore the sensitivity of surface scattering strength to environmental variables as functions of the acoustic frequency and scattering angles.

Data Sources

The deep-water data used in the nonlinear, multiparameter curve fitting of the SSS model derive from a variety of sources: Bachmann; Brown et al.; Chapman and Harris; Chapman and Scott; Crowther; and Ogden and Erskine—see the references of Refs. 53 and 58. (The curve-fitting is done using dB values.)

For low frequencies (<1500 Hz), the primary data were broadband SUS data from CST-4 and CST-7 Phase 2, two experiments conducted in the Gulf of Alaska. In both of them, in situ measurements of bubble-cloud properties were made, and the fish contributions to the scattering are considered to be well understood [45].

Interface Scattering Model

A bistatic scattering model for σ_{int}^{surf} was described above. Here, we illustrate its sensitivities to its inputs, and derive a simplified model that depends environmentally only on the wind speed (and c_0).

Model Illustrations

Figure 16 presents representative frequency and grazing-angle behaviors of σ_{int}^{surf} that hold for most wind speeds.

Figures 16(a) and 16(b) illustrate the generally moderate frequency dependence of air-sea interface scattering. In each plot, the three sets of curves correspond to grazing angles of 10° , 30° , and 60° for a wind speed of 20 m/s. (Similar behavior was seen at most wind speeds.) Figure 16(a) shows that, as expected from the definition of $W(Q_h)$, the strongest dependence is for $\gamma_2 = 3.0$, with levels rising ~ 20 dB as the frequency increases from 100 to 10000 Hz, and the weakest dependence is for $\gamma_2 = 3.9$ (~ 1 dB increase). This is reinforced in Fig. 16(b), where γ_2 is fixed at 3.9 and A_S is allowed to vary. (Recall the only frequency dependence in our σ_{int}^{surf} model comes from γ_2 .) Figure 16(b) also shows a basically linear, monotonically increasing dependence on A_S at low angles, with a more complex behavior at high angles.

Figures 16(c) and 16(d) show the very strong dependence of σ_{int}^{surf} on grazing angle, with levels increasing by 50 dB or more as the grazing angle is increased from 5° to 60° . (This behavior holds over a wide range of environmental values and frequencies.)

Re the grazing-angle sensitivity of σ_{int}^{surf} to γ_2 and A_S , Figs. 16(c) and 16(d) show that increasing the value of each parameter leads to increasing σ_{int}^{surf} at lower grazing angles, while at higher angles, the picture is more complicated. Near specular, increasing the value of each parameter in fact leads to decreasing σ_{int}^{surf} . (For scattering from rough surface, these angular trends are not unexpected.) Figure 16(a) further shows that for a given A_S , the angular regions where there will be a monotonically increasing or decreasing dependence of σ_{int}^{surf} on γ_2 will be frequency-dependent.

Simplified Model

With the goal of constructing a SSS model that depends environmentally on only the wind speed U (and c_0), this σ_{int}^{surf} model was fit to low sea-state CST-4 and CST-7 Phase 2 data to derive estimates of the model's two surface-wave spectral parameters. The resulting best-fit values were $\gamma_2 = 3.8$ and $A_S = 1.9 \times 10^{-4} \text{ m}^3\text{-s}$. (Initial comparisons with in situ wave spectral values have been favorable [60-61].)

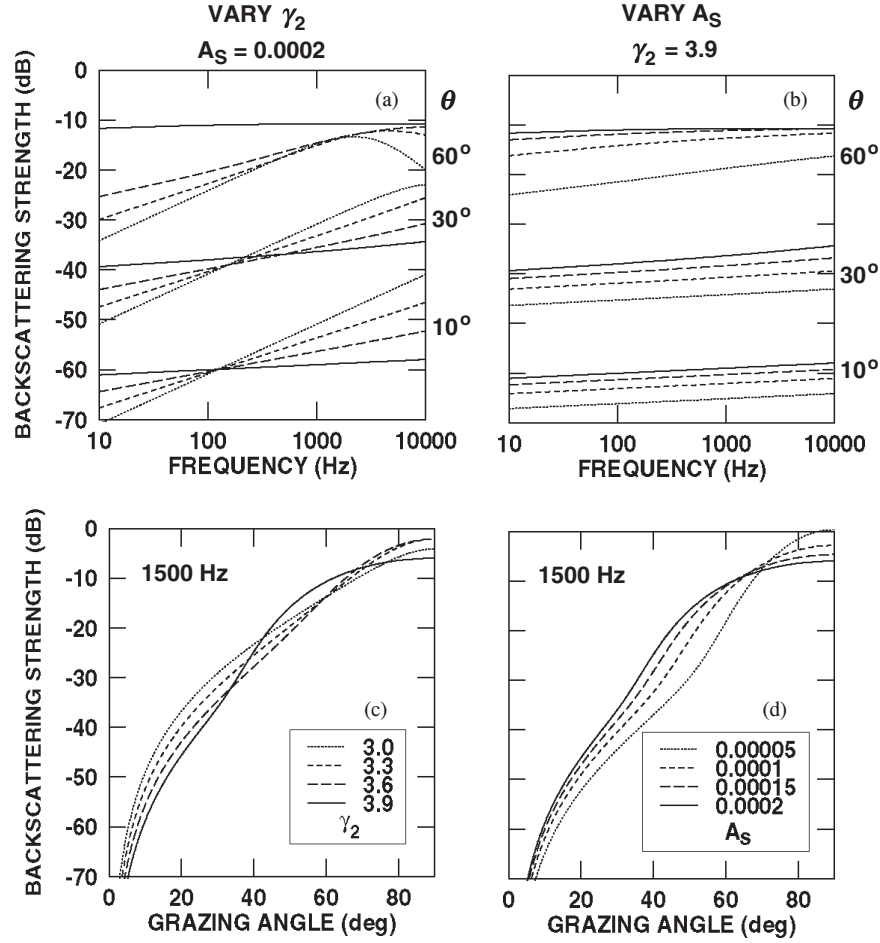


Fig. 16 — Monostatic predictions of interface backscattering strength at $U = 20$ m/s as a function of (a)-(b) frequency and (c)-(d) grazing angle, for two sets of surface wave spectral variables. In (a) and (c), $A_S = 0.0002$ m³-s, and in (b) and (d), $\gamma_2 = 3.9$.

Given that the γ_2 derived from fitting the acoustic data was 3.8, Fig. 16 suggests that σ_{int}^{surf} will generally have a mild frequency dependence (at least in the open ocean). This is illustrated in Fig. 17, which provides a representative example from CST-7 Phase 2 of broadband, low-wind-speed scattering strengths observed during the CST series of experiments.

Bubble-Cloud Scattering Model

Figure 18 provides a low-frequency example of how the surface backscattering strength can change when wave breaking is significant. In this high-wind-speed example from CST 7 Phase 2, we see the strongly enhanced scattering levels relative to those predicted as being due to the air-sea interface (black curves). We also note that in this case, the maximum response is not at the highest frequency, but at 962 Hz, and that, even at 82 Hz, the presence of bubbles contributes significantly to the backscattering. We now describe a bistatic σ_{bub} model that attempts to capture these features.

The bubble-cloud scattering prediction derives from the stochastic model of Gilbert [66]. In Ref. 66, the mean bubble-cloud backscattering cross section is modeled as a product of an effective horizontal wavenumber spectrum and a “geometric factor.” (However, as Gilbert notes, very little is known about the former.) This geometric factor describes how the backscatter intensity from a bubble cloud depends on two competing factors:

- The rapid decrease of average air-void fraction with depth, which suggests that most scattering occurs very close to the surface; and

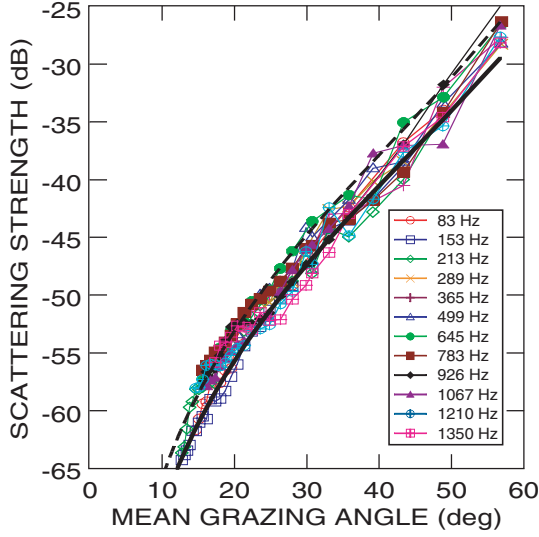


Fig. 17 — Low-wind-speed surface scattering strengths measured in the Gulf of Alaska during CST-7 Phase 2 (February 1992). The wind speed was 4.5 m/s. The acoustic data were collected quasi-monostatically using omnidirectional explosive charges as sources, which detonated at depths of ~ 540 m below a horizontal receiver towed at a depth of ~ 220 m. Overlaying the data are bistatic SSS model predictions (with $A_S = 0.00019$ $\text{m}^3\text{-s}$, $\gamma_2 = 3.8$) at 83 Hz (thick black, solid curve) and 1350 Hz (thick black, dashed curve).

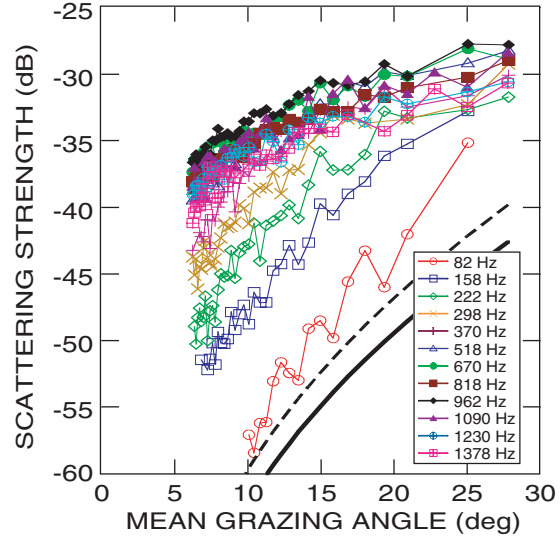


Fig. 18 — High-wind-speed surface scattering strengths measured in the Gulf of Alaska during CST-7 Phase 2 (February 1992). The wind speed was 17.9 m/s. The acoustic data were collected quasi-monostatically using omnidirectional explosive charges as sources, which detonated at depths of ~ 560 m below a horizontal receiver towed at a depth of ~ 260 m. Also plotted are bistatic σ_{int}^{surf} model predictions (with $A_S = 0.00019$ $\text{m}^3\text{-s}$, $\gamma_2 = 3.8$) at 82 Hz (thick black, solid curve) and 1378 Hz (thick black, dashed curve).

- The vanishing of the total acoustic field at the surface and its increase to a maximum several meters below the surface, because of interference between the incident and surface-reflected waves (Lloyd's mirror pattern).

Assuming that a bubble cloud may be modeled as a vertical distribution of uncorrelated point scatterers (at depths z), the convolution of these two effects in the monostatic case leads to a total intensity of [66]

$$I = \int_0^\infty A_1 \sin^4(k_0 z \sin \theta) \exp(-2z/d) dz = A_2 k_v^4 d^5 / [(1 + k_v^2 d^2)(1 + 4k_v^2 d^2)] \quad (40)$$

where d is the e-folding depth of the air fraction, $k_v \equiv k_0 \sin \theta$ is the magnitude of the vertical wavenumbers of both the incident and scattered fields, and the A_i are scaling factors.

The approach we have taken is to use the above geometric factor as a starting point for a new bistatic σ_{bub} algorithm. First, Eq. (40) was extended to 3D geometries [67]. Then, the scaling factor was taken to be a three-parameter function of k_0 and d . To determine these three σ_{bub} parameters, we needed a ready means of estimating d . Fortunately, there is a prescription relating d to the wind speed U . Based on measurements during CST-7 Phase 2, Farmer and Vagle have derived the following empirical formula [54]:

$$\begin{aligned} d &= 0.557 - 0.117 \cdot U + 0.0109 \cdot U^2 & U > 7.5 \text{ m/s,} \\ &= -0.19509 + 0.06503 \cdot U & 3 \leq U \leq 7.5 \text{ m/s,} \\ &= 0 & U < 3 \text{ m/s.} \end{aligned} \quad (41)$$

Using this formula, multidimensional, nonlinear regression routines were then used to fit our SSS model to the full data set (over 10000 data points). (Because no in situ measurements of d were made during the non-CST-7 Phase-2 measurements, Eq. (41) was assumed to hold for all the acoustic data.) The result is [59]

$$\sigma_{bub} = \frac{0.0019d^{5.15}k_0^{-0.6}k_{v,i}^2k_{v,s}^2[6+3(k_{v,i}^2+k_{v,s}^2)d^2+(k_{v,i}^2-k_{v,s}^2)^2d^4]}{2(1+k_{v,i}^2d^2)(1+k_{v,s}^2d^2)[1+(k_{v,i}-k_{v,s})^2d^2][1+(k_{v,i}+k_{v,s})^2d^2]}, \quad (42)$$

where $k_{v,i} \equiv -k_0 \sin \theta_{inc}$ and $k_{v,s} \equiv -k_0 \sin \theta_{scat}$. As with the 3D σ_{fish}^{surf} and σ_{fish}^{bot} models, the point-scatterer and flat-interface assumptions imply that, to first order, σ_{bub} depends on θ_{inc} and θ_{scat} , but not ϕ_{bi} .

Thus, for this model, σ_{bub} depends on two environmental parameters: d and c_0 , which, via a further approximation (Eq. (41)), becomes just U and c_0 .

Comments

For practical applications of this model as kernels in reverberation or performance models, a field of discrete bubble clouds is treated as a spatially (and temporally) uniform layer, which in turn is treated as an effective modifier of surface properties. (Being a semi-empirical model, the nonuniform nature of real bubble fields is already embedded in the derived values of the σ_{bub} parameters.) Hence, it can be used as a surface scattering strength with no need to introduce a separate layer into the modeled waveguide.

Model-Model Comparisons

The residual standard error r_{se} for fitting the resultant new SSS model to the full deep-water data set was 2.4 dB, compared to 4.1 dB when applying the Chapman-Harris [64] empirical formula. (When restricted to data corresponding to frequencies below 1000 Hz, the new model had an r_{se} of 2.2 dB, compared to 4.1 and 3.1 dB when applying the Chapman-Harris and Ogden-Nicholas-Erskine [65] empirical formulas, respectively.)

Simplified SSS Model

We have just derived a SSS model that relies environmentally on just U and c_0 . However, as the dependence on $c_0 \in [1400, 1600]$ m/s is typically weak, it could be hardwired at 1500 m/s, with only minor ($< \sim 1$ dB) effects on SSS. Doing so, the result is a simplified SSS model that depends environmentally on only the wind speed.

Model Illustrations

With Fig. 19 we begin to look at the relative contributions of bubble clouds and the interface to surface scattering strength. Figures 19 through 22 present monostatic predictions, while Fig. 23 presents bistatic predictions. For the predictions of interface scattering, we set $A_s = 0.0002$ m³-s and $\gamma_2 = 3.9$ since, of the parameter values of Fig. 16, they are the most representative of open-ocean values. (In Figs. 19 through 23, there are no bubble-cloud scattering predictions for wind speeds less than 3 m/s, as our model assumes $\sigma_{bub} \equiv 0$ for $U < 3$ m/s. For all predictions, we take $c_0 = 1500$ m/s and $\phi_{bi} = 180^\circ$.)

Grazing-Angle Dependence

Figure 19 displays the grazing-angle dependence at 1500 Hz for five wind speeds (2.5, 5, 10, 15, and 20 m/s) of bubble-cloud scattering strength (Fig. 19(a)), interface scattering strength (Fig. 19(b)), and the sum of the two, SSS (Fig. 19(c)). Figure 19(a) illustrates the relatively flat grazing angle dependence of bubble-cloud scattering, and that the range of grazing angles over which the flatness occurs increases with increasing U . It also shows the especially strong dependence of σ_{bub} on U at low grazing angles ($< \sim 30^\circ$ at 1500 Hz).

In contrast, σ_{int}^{surf} has both a milder and more complex dependence on U as a function of grazing angle (Fig. 19(b)), with σ_{int}^{surf} increasing with U at the lower angles and decreasing with U near specular (as would be expected as the surface becomes increasingly rougher).

The combination of effects (Fig. 19(c)) reinforces the general rule of thumb that bubble clouds dominate the scattering at low grazing angles (when wave breaking is significant) and the rough air-sea interface at high angles, with a wind-speed-dependent mix at moderate angles.

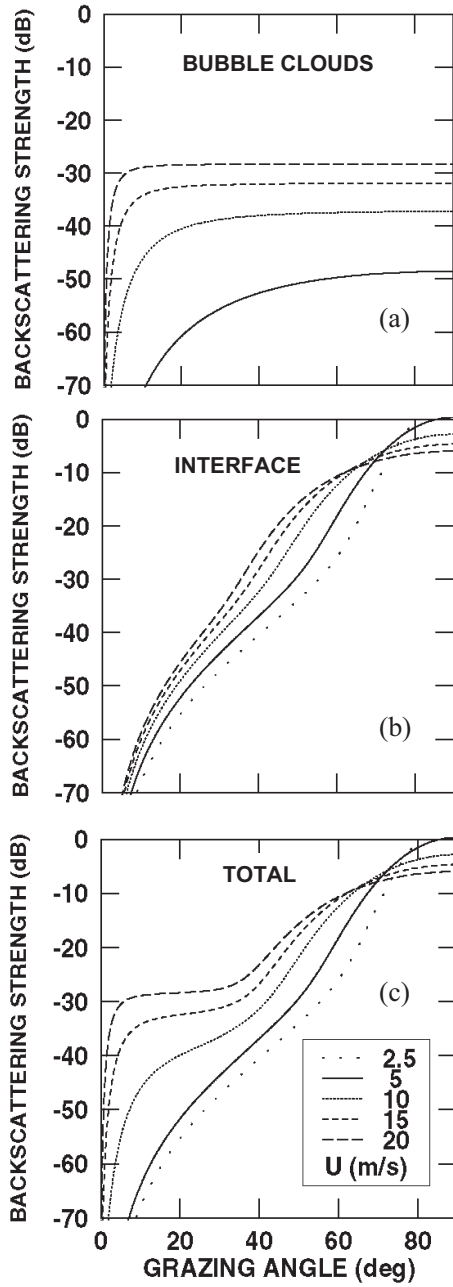


Fig. 19 — Monostatic predictions of surface backscattering strength at 1500 Hz as a function of grazing angle for five wind speeds. (a) Bubble-cloud backscattering strength; (b) and (c) correspond to interface and total (bubble-cloud + interface) backscattering strength, respectively, assuming $A_S = 0.0002 \text{ m}^3\text{-s}$ and $\gamma_2 = 3.9$.

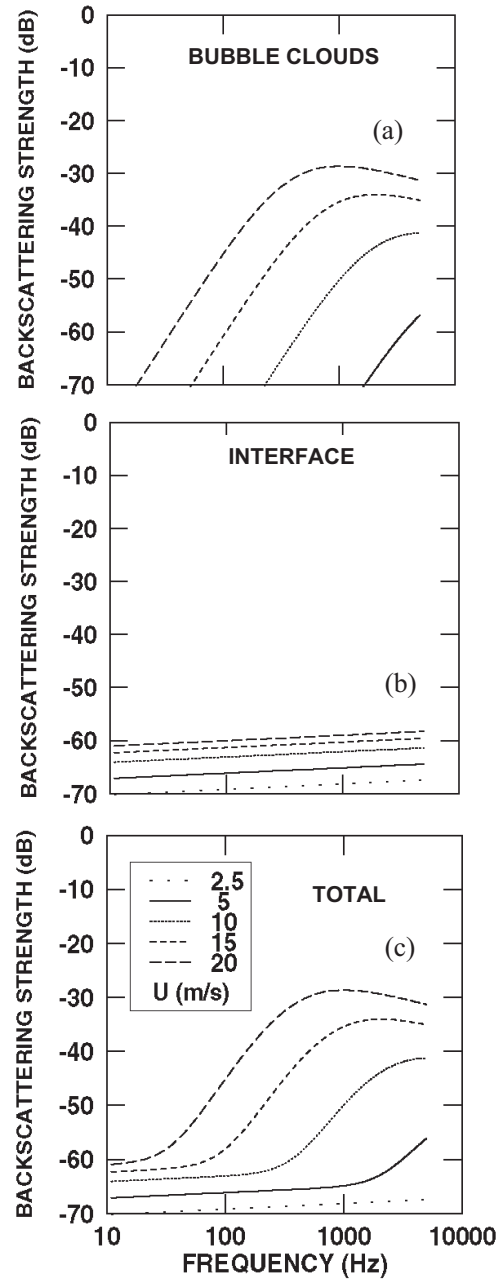


Fig. 20 — Monostatic predictions of surface backscattering strength at $\theta = 10^\circ$ as a function of frequency for five wind speeds. (a) Bubble-cloud backscattering strength; (b) and (c) correspond to interface and total (bubble-cloud + interface) backscattering strength, respectively, assuming $A_S = 0.0002 \text{ m}^3\text{-s}$ and $\gamma_2 = 3.9$.

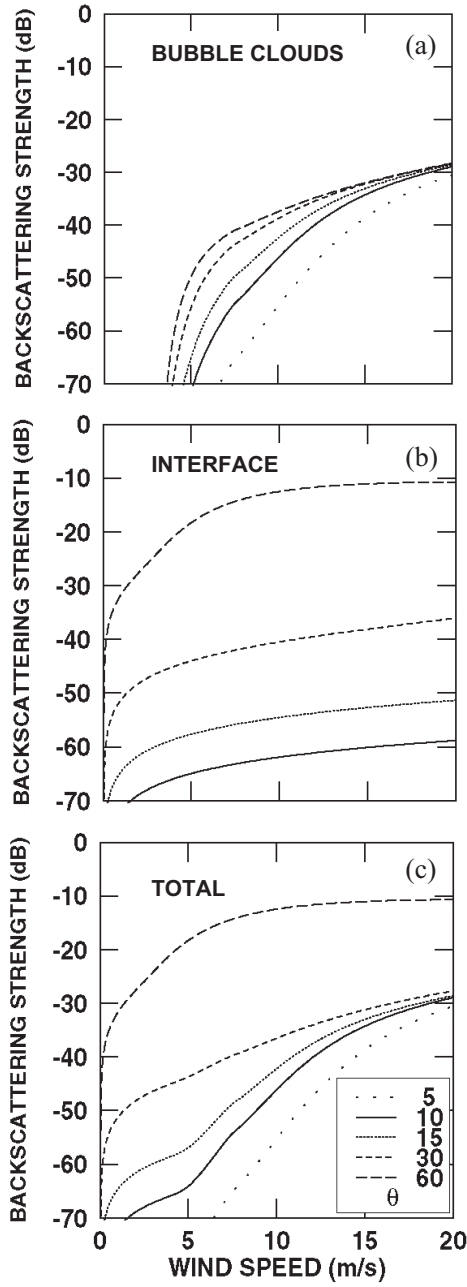


Fig. 21 — Monostatic predictions of surface backscattering strength at 1500 Hz as a function of wind speed for five grazing angles. (a) Bubble-cloud backscattering strength; (b) and (c) correspond to interface and total (bubble-cloud + interface) backscattering strength, respectively, assuming $A_S = 0.0002 \text{ m}^3\text{-s}$ and $\gamma_2 = 3.9$.

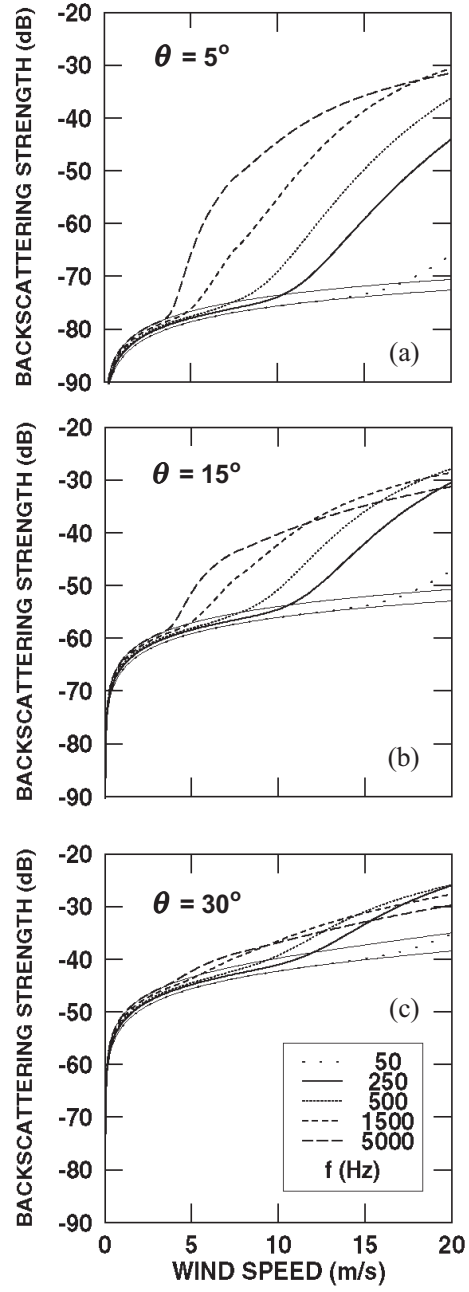


Fig. 22 — Monostatic predictions of surface backscattering strength at three grazing angles as a function of wind speed for five frequencies. For comparison, monostatic predictions of just the contributions due to the air-sea interface at 50 and 5000 Hz (thin solid curves) are included in each subplot. (The interface-scattering predictions assumed $A_S = 0.0002 \text{ m}^3\text{-s}$ and $\gamma_2 = 3.9$.)

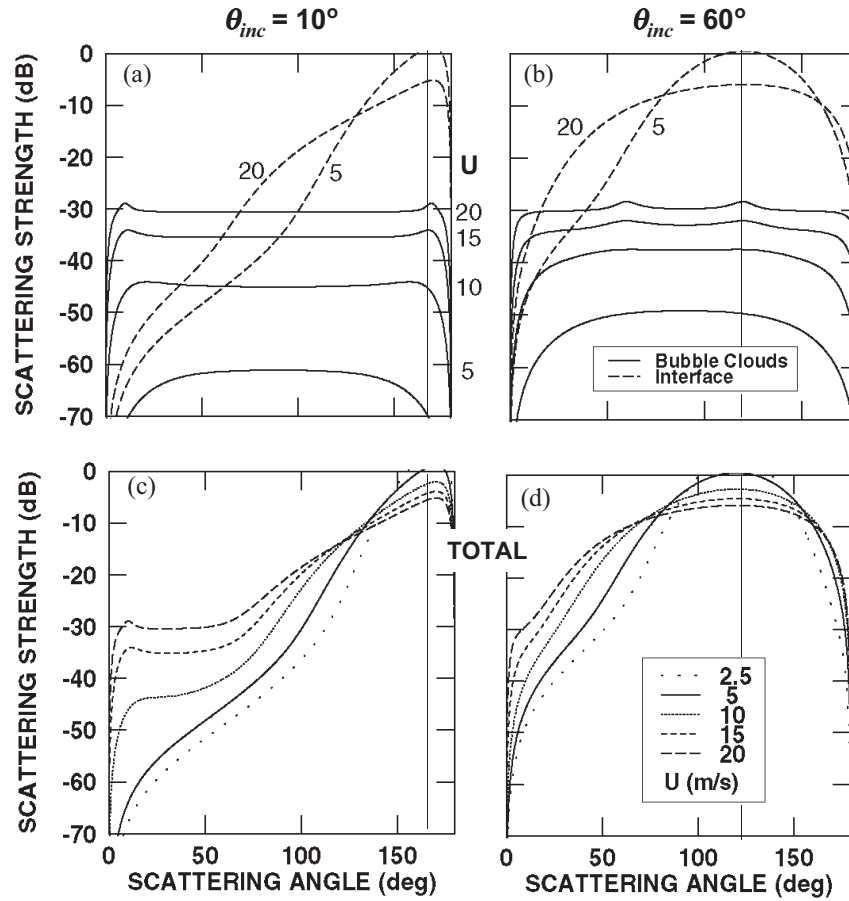


Fig. 23 — Modeled bistatic surface scattering strengths at 1500 Hz as a function of scattered grazing angle θ_{scat} for two incident grazing angles. In (a)-(b), bubble-cloud scattering strength is shown (solid curves) for four wind speeds ($U = 5, 10, 15$, and 20 m/s) and interface scattering strength (dashed curves) for two winds ($U = 5$ and 20 m/s), assuming $A_S = 0.0002 \text{ m}^3\text{-s}$ and $\gamma_2 = 3.9$. In (c)-(d), the total (bubble-cloud + interface) scattering strength is shown for five wind speeds. (The dashed vertical lines indicate the specular directions in each case.)

Frequency Dependence

Figure 20 shows the dependence of SSS at low grazing angles on frequency and wind speed. As in the previous figure, Fig. 20(a) corresponds to bubble-cloud scattering, Fig. 20(b) to interface scattering, and Fig. 20(c) to the sum of the two (SSS). Again, the set of five curves in each plot corresponds to five wind speeds (2.5, 5, 10, 15, and 20 m/s). A grazing angle of 10° is picked as an interesting one where both bubble clouds and the interface can have a significant influence on the acoustics.

Figure 20(a) illustrates the strong frequency-dependence of bubble-cloud scattering below 1 kHz, with a peak occurring at a frequency that decreases with increasing wind speed. (Both points are dramatically illustrated in Fig. 18, with peak acoustic response in this case at 962 Hz.) Above 1 kHz, the frequency dependence is relatively mild for wind speeds greater than 10 m/s. Figure 20(b) shows that, for our given wave spectrum, the frequency and wind speed dependence of interface scattering are fairly benign. (For a different wave spectrum, the wind-speed dependence would be similar to those in Fig. 20(b), although the curves would exhibit a different dependence on frequency (Fig. 16(a)) and/or be at displaced levels (Fig. 16(b).))

The effects of including both scattering mechanisms are shown in Fig. 20(c). At this grazing angle, at wind speeds above 10 m/s, bubble-cloud scattering dominates above ~ 250 Hz. Below 10 m/s, surface scattering

strength can be due to a combination of bubble-cloud and interface scattering, while below 5 m/s, interface scattering dominates (except at high frequencies). As the grazing angle increases, interface scattering becomes increasingly dominant (Fig. 19).

Wind-Speed Dependence

Figure 21 illustrates the wind-speed dependence of SSS as a function of grazing angle. As in the previous figure, Fig. 21(a) corresponds to bubble-cloud scattering, Fig. 21(b) to interface scattering, and Fig. 21(c) to the sum of the two (SSS). In this case, the set of five curves in each plot corresponds to five grazing angles (5, 10, 15, 30, and 60 deg). A frequency of 1500 Hz is picked as an interesting one in which both bubble clouds and the interface can have a significant influence on the acoustics.

Figure 21(a) illustrates the very strong wind-speed dependence of bubble-cloud scattering strength, especially in the regime from when wave breaking becomes significant ($U \sim 5$ m/s for 1500 Hz) until the onset of high sea states ($U \sim 15$ m/s for 1500 Hz), where σ_{bub} begins to appreciably slow its increase. In Fig. 21(b), equivalent curves are presented for interface scattering strength; these reflect our previous comments as to interface scattering's strong grazing-angle and relatively mild wind-speed dependence (compared to those of bubble-cloud scattering).

Figure 21(c) shows the general dominance of interface scattering at high grazing angles and that of bubble-cloud scattering at low grazing angles in moderate-to-high winds. The contrast among these three figures shows the complexity of surface scattering at low-to-moderate winds and low grazing angles; the frequency dependence of σ_{bub} adds to the fun.

Figure 22 again plots the dependence of SSS on wind speed, but this time as a function of frequency at three low grazing angles. This figure reinforces the points that bubble clouds become an increasingly important driver of backscattering strength with both increasing frequency and wind speed, and with decreasing grazing angle. For example, at a grazing angle of 5°, the contribution of bubble-cloud backscattering to SSS for frequencies $> \sim 1$ kHz can be 30 to 40 dB higher than the contribution of air-sea-interface backscattering for wind speeds in excess of 15 m/s.

Bistatic-Angle Dependence

Figure 23 illustrates that the general trends discussed so far extend to bistatic geometries. In these examples at 1500 Hz, bubble-cloud and interface scattering strengths (Figs. 23(a-b)), and their total (SSS) (Figs. 23(c-d)), are shown for a set of wind speeds for two incident grazing angles of 10° and 60° (thus, specular is at 170° and 120°, respectively).

A comparison of Figs. 23(a) and 23(c) with Fig. 19 shows that, in general, at high scattering angles (toward specular), interface scattering dominates, while at low scattering angles, bubble-cloud scattering dominates for wind speeds of 10 m/s and greater. This is emphasized in Figs. 23(b) and 23(d), where the incident grazing angle has been increased to 60°, with the expected result that interface scattering dominates over a larger range of scattering angles and wind speeds.

Comments

We have presented a new semi-empirical broadband surface scattering strength formula parameterized environmentally by the wind speed, two surface-wave spectral parameters, and the air-void fraction e-folding depth d . Further approximations led to a formula whose sole environmental parameter is the wind speed U . From an analysis of the variance of CST-4 and CST-7 Phase 2 SSS 's measured during periods of similar wind speeds (~ 9 to 11 m/s), it can be shown that wind speed is not the whole story. (For example, the relative wind and wave directions can potentially be of significance: Farmer and Vagle have found [54] enhanced wave breaking (bubble generation) when the wind direction changes, and reduced wave breaking when the wind and wave directions are opposed.) Hence, to provide more accurate predictions of σ_{bub} , in situ measurements of d and other environmental measures of the air-sea boundary conditions will be necessary. Furthermore, it should

be noted that the relationship between d and U can depend on the site and the season [54], so that physics-based versions of this relationship need to be developed.

The SSS model presented should be viewed as an interim model. For example, we are considering different roughness spectra for the σ_{int}^{surf} model, and are trying other functional forms for s_{bub} . We also need to properly include the coherent component in the σ_{int}^{surf} model to predict forward scattering (surface loss). (Our new model for dispersed-fish scattering in the presence of the sea surface is contributing to the ongoing effort to definitively identify the relative contributions of bubbles, waves, and fish in low-to-moderate sea state data from the CST and other archival data sets.)

Subtle differences in low- and mid-frequency SSS characteristics (such as in grazing angle behavior) were observed when separately deriving fits for data above and below 1500 Hz. These phenomena (perhaps suggestive of different scattering physics) are under study.

7. CONCLUSIONS

These new bistatic scattering strength models should help advance the accuracy and robustness of predictions of multistatic active sonar performance. By having a physics basis, the models allow extrapolation in frequency and to most 3D geometries. Hence, they should be particularly useful for shallow-water applications where a wide variety of scattering angles is encountered, but where making controlled measurements of scattering strength is difficult. Our models' broadband and bistatic natures permit their application to a wide range of multistatic active sonar systems and concepts.

The models have proved essential for isolating scattering mechanisms and thereby advancing our understanding of the complex acoustic interaction processes at the ocean boundaries. (For example, being able to systematically identify and remove fish-scatter contributions from surface-scatter data has, in turn, led to more accurate surface-scattering models.)

Because of their basis in physical theory, these models can be used as inversion ("remote-sensing") tools. (For example, fits of the interface surface scattering model to broadband, low-wind-speed acoustic data were used to back out representative surface-wave spectral values.) For algorithm development and in situ operations, these models have several potential uses:

- Benchmarking geo-acoustic inversion and environmentally adaptive (EA) algorithms
- Forming the basis for "next-generation" EA techniques
- Extrapolation in frequency and angle (especially bistatically), given an environmental parameter estimation from a small band of angles at a few frequencies
- Helping to invert for hard-to-estimate geophysical parameters (such as the spectral strength and exponent of bottom roughness)
- Identifying what oceanographic and geophysical quantities need to be measured, and to what accuracy
- Serving as a guide to expected acoustic behavior (e.g., identifying when elastic effects are significant)
- Serving as a guide in asset choice and deployment, and frequency and waveform selection (optimizing signal-to-interference ratios).

Despite their apparent complexity in some cases, the models are straightforward to code and run quite quickly (especially if vectorized—we have MATLAB[®] and/or S-PLUS[®] codes for all models).

In general, measures of sonar performance depend nonlinearly on the reverberation, which in turn depends nonlinearly on the environmental (oceanographic, geophysical, and biological) variables. A key benefit of these models is that they allow a systematic determination of the relative influence of these environmental inputs on the strength of the acoustic scattering. In turn, used as scattering submodels in active sonar performance models, they allow a more accurate estimation of the relative influence of the environment on sonar performance.

Furthermore, by independently varying the values of the environmental parameters, the resultant impact on the scattering can be estimated in a statistical sense. Hence, the relative variability or uncertainty in sonar

performance can be assessed, and the expected variance modeled (i.e., helping to estimate reverberation probability density functions).

We now provide a categorized list of the major points and recommendations of the paper:

General Interface Scattering

Bottom and surface interface scattering were well-modeled by the SSA. Its use is strongly recommended over empirical (such as Lambert's or Lommel-Seeliger's law for the bottom) and PT approaches.

To more accurately model scattering strength at high scattering angles and in the specular direction, the pure power-law wave spectrum needs to be modified to include a low-wavenumber cut-off. Furthermore, for the sea surface, more general, directional water-wave spectra need to be incorporated into the scattering model. (These efforts are underway at NRL.)

Bottom Interface Scattering

Scattering from the bottom interface has a complex and strong dependence on the incident and scattered grazing angles, and on the geophysics. Of the latter, at low grazing angles the spectral parameters, sound speeds and density will typically have the most influence on the acoustics. (Generally, the harder the bottom, the stronger the acoustic response at low scattering angles.) The dependence of the scattering response on acoustic frequency is generally monotonic, with levels typically increasing moderately with increasing frequency.

Elastic effects can be significant below the critical angle for bottom-interface scattering from shear-supporting bottoms, i.e., skin effects due to evanescent shear waves can be significant. Surface roughness enhances these effects. (Our SSA model has the advantage of accurately predicting such effects in cases where the acoustic wavelength cannot resolve violations of the single-valuedness assumption implicit in the "rough-surface" assumption.) One particular manifestation is shear-induced nulls in scattering strength at low grazing angles. As illustrated with the mudstone example from the Oregon coast, these nulls can occur even when the shear speed is well below the water sound speed.

Volume Scattering

Bladdered fish can be significant scatterers at low grazing angles, even at relatively low densities. When they are near the ocean surface or bottom, their scattered intensity can be significantly altered (by a factor between 0 and 16; typically 4). This response depends strongly on the incident and scattered grazing angles, the distance of the scatterers from the boundary, the acoustic frequency, and for the ocean bottom, its physical properties. Due to the more reflective nature of the ocean surface, near-surface fish will elicit a more variable response than near-bottom fish.

Near-ocean-surface fish can be a significant and complex low- and mid-frequency scattering mechanism. For example, they, and not bubbles, may in fact be responsible for reported deviation of low-frequency surface scattering strengths at low grazing angles from rough-surface scattering predictions in low and moderate sea states.

Similarly, near-ocean-bottom fish could be responsible, in some cases, for scattering attributed to interface and/or sediment-volume scattering. (Recall the above scattering strength data with a $\mu \sin \theta$ dependence that suggested a coincidental combination of rockfish scattering at low grazing angles, and mudstone bottom scattering at intermediate angles.) As was demonstrated, bladdered fish very near the bottom (or even resting on it) can still be appreciable scatterers. Furthermore, because of their often high spatial variability in shallow water, local "hot spots" of near-bottom fish could be mistaken for "geoclutter".

In general, fish will be of more importance as a source of interference to active sonar systems at mid-frequencies and in shallow water. The strength of volume scattering will be strongly dependent on local

conditions (such as the types, number densities, sizes, and depths of fish present, and the time of day). Furthermore, their spatial and temporal variability will in turn lead to acoustic variability.

Surface Scattering

A surface scattering strength model was presented that offers significant advances over previous (purely empirical, monostatic) algorithms in several ways: (a) the scattering descriptions of both the rough air-sea interface and subsurface bubbles derive from fundamental physics; (b) the algorithms that implement them operate in 3D mode; and (c) the resulting models apply over a broader frequency range (which includes ASW frequencies). (Furthermore, for scenarios where the models all apply, the new model more accurately fits the observed data.) While this model represents a considerable improvement in predictive capabilities, it should be noted that it is still semi-empirical, with a significant amount of its key oceanographic and low-frequency acoustic data deriving from one open-ocean location at basically one time of the year.

Scattering due to bubble clouds can be dominant at low grazing angles when wave breaking is significant. Bubble clouds become an increasingly important driver of backscattering strength with both increasing frequency and wind speed, and with decreasing grazing angle. For quantitative predictions, a good estimate of the in situ wind speed is needed. (Wind-history effects are relatively unimportant.) Bubble cloud scattering typically has a relatively flat response with grazing angle (especially for wind speeds above 10 m/s). The range of angles where the response is flat increases with both wind speed and frequency. Bubble-cloud scattering has a strong dependence on frequency below ~1 kHz (with a relatively flat response above for wind speeds in excess of 10 m/s).

Scattering due to the rough air-sea interface depends most strongly on the scattering angle and environmental conditions. To predict its strength, a good estimate of the surface wave spectrum, primarily at short wavelengths, is needed. At large scattering angles, the interface is the dominant surface-scattering mechanism at all frequencies, even in high sea states. Interface scattering has a relatively mild dependence on environmental parameters. (σ_{bub} will be much more responsive to locally changing oceanographic conditions, such as an increase in wind speed, than will σ_{int}^{surf} .)

A key feature of the surface scattering strength model presented is its environmental reliance on readily observable oceanographic variables, which in turn offers the potential for accurate predictions of SSS in near-real-time on regional scales through the use of remote sensing. (The accuracy and availability of real-time, wide-area measures of these variables are continually improving [62-63].)

For most frequencies and sea conditions, the model results demonstrated that at low scattering angles, the key environmental quantity to be measured is the wind speed. At moderate-to-high scattering angles, bubble-cloud scattering is less important. In this regime, both the wind speed and directional wave spectra need to be measured.

Issues

While these models provide improved predictions of *mean* (incoherent) scattering levels, technical issues remain. A primary need is high-quality acoustic and environmental data to provide the ground truth necessary to rigorously evaluate the models, and to assess the generality and limitations of their physical assumptions. For each interface, the coherent (specular) component needs to be properly combined with the incoherent component to accurately predict boundary loss. Specific issues include:

Bottom Scattering

We have explored in this paper how the properties of the bottom drive the acoustics. To improve the accuracy and robustness of bottom-scattering models, much work remains:

- Wide ranges of measured acoustic and geophysical values have been observed, even in environments of similar “bottom type” (e.g., sand). Bottom properties are often difficult to measure in situ to the level of

detail required by models—needed are new measurement techniques to characterize the bottom. This, in particular, includes measuring interface roughness.

- Consequently, scattering-model validation at low- and mid-frequencies is poor, principally due to the lack of high-quality, *concurrent* acoustic and geophysical measurements. (There is a particular sparsity of 3D acoustic data.)
- The statistics of sediment-volume scattering is not well understood—needed are 3D geologic models of sediment heterogeneities.
- How significant is subcritical angle penetration due to surface roughness [68] at low- and mid-frequencies?
- For acoustic measurements, it is difficult in shallow water to isolate direct-path scattering (particularly at low frequencies and angles) [36]. Range dependence makes it even tougher.

Volume Scattering

To predict the scattering contributions from fish in a given environment, knowledge of fish behavior as well as fish types and densities are required. (For example, knowing the diurnal depth behaviors and seasonal migration patterns of particular fish species can aid greatly both in predicting their acoustic behavior on regional scales, and in mitigating their influence on sonar performance.) Particular issues include:

- Modeling the dynamism of fish and fish schools in shallow water to whatever accuracy is realistically possible.
- Developing the capability for at-sea assessments of fish school statistics.
- Developing and validating fish school scattering models that incorporate effects due to the presence of the ocean boundaries.

Surface Scattering

To provide more accurate predictions of scattering from bubble clouds, in situ measurements of the air-void fraction and other environmental measures of the air-sea boundary conditions will be necessary. Hence, the air-void fraction represents a candidate quantity for estimation with remote-sensing technologies (perhaps using lidar). The relationship(s) between the air-void fraction and the wind speed (and other environmental descriptors) can be site and seasonally dependent [54], so that physics-based models of the Bragg-scale structure of the void fraction need to be developed.

To provide more accurate measurements of scattering from the air-sea interface, in situ estimates of 2D surface-wave power spectra are needed (e.g., via synthetic aperture radar (SAR) imagery).

A deeper understanding of bubble properties near the surface is needed. Important outstanding questions include:

- What properties of bubbles drive the acoustics?
- How are they affected by environmental conditions such as temperature and salinity?
- How do they evolve temporally? Spatially?
- At what frequencies are individual resonant bubbles important? Clouds of bubbles? What are the relative roles of attenuation and Bragg scattering generated by heterogeneities in the sound-speed profile as a function of frequency and sea state?
- What are the differences between the open ocean, shallow water, and the surf zone? (In coastal waters, SSS levels are often significantly enhanced [58].)
- How do surface waves couple into the problem?
- What is the relationship between scattering and noise?

Recommendations

We close with some recommendations for any scattering measurement:

- Maximize the frequency and grazing-angle (both incident and scattered, if possible) coverage to sort out scattering mechanisms and help invert for environmental parameters.
- Perform day/night measurements to help sort out the fish contributions.

ACKNOWLEDGMENTS

This work was supported by the Office of Naval Research.

REFERENCES

1. J.L. Hanson, "Winds, Waves and Bubbles at the Air-Sea Boundary," *Johns Hopkins APL Tech. Dig.* **14**, 200-208 (1993).
2. R.H. Love, "Resonant Acoustic Scattering by Swimbladder-Bearing Fish," *J. Acoust. Soc. Am.* **64**, 571-580 (1978).
3. R.W. Nero, "A Phenomenological Model to Predict the Density and Distribution of Pacific Hake by Season and Geography," NRL/FR/7180—00-9697, Naval Research Laboratory, Stennis Space Center MS, March 2000.
4. C. Feuillade, R.W. Nero, and R.H. Love, "A Low-Frequency Acoustic Scattering Model for Small Schools of Fish," *J. Acoust. Soc. Am.* **99**, 196-208 (1996).
5. R.C. Gauss, R.W. Nero, and D. Wurmser, "A Lloyd-Mirror Model to Estimate the Scattering Strength of Fish Near Rough Ocean Boundaries," *J. Acoust. Soc. Am.* **104**, 1820 (A) (1998).
6. J.D. Zittel, F.T. Erskine, C.W. Holland, A.I. Eller, R.J. Soukup, B.E. Raff, and W.T. Ellison, "Critical Sea Test Final Report," SPAWAR CST/LLFA-WP-USWAC-9, Johns Hopkins University, Applied Physics Laboratory, Laurel, MD, September 1996.
7. C.H. Spikes, F.T. Erskine, J.F. McEachern, and D.H. Backes, "Littoral Warfare Technology Testing," *Sea Technol.* **38**, 71-77 (1997).
8. D.R. Jackson, "A Model for Bistatic Bottom Scattering in the Frequency Range 10-100 kHz," APL-UW TR 9305, Applied Physics Laboratory, University of Washington, Seattle, WA, August 1993.
9. A.G. Voronovich, "Theory of Sound Scattering by a Free Corrugated Surface," *Sov. Phys. Acoust.* **30**, 444-448 (1984).
10. A.G. Voronovich, "Small-Slope Approximation in Wave Scattering by Rough Surfaces," *Sov. Phys. JETP* **62**, 65-70 (1985).
11. A.G. Voronovich, "A Unified Description of Wave Scattering at Boundaries with Large and Small Roughness," in *Progress in Underwater Acoustics*, edited by H.M. Merklinger, 16-18 July 1986, Halifax, Nova Scotia, Canada (Plenum Press, New York, NY, 1986), pp. 25-34.
12. R. Dashen, F.S. Henyey, and D. Wurmser, "Calculations of Acoustic Scattering from the Ocean Surface," *J. Acoust. Soc. Am.* **88**, 310-323 (1990).
13. D. Wurmser, "A Manifestly Reciprocal Theory of Scattering in the Presence of Elastic Media," *J. Math. Phys.* **37**, 4434-4479 (1996).

14. E.I. Thorsos, "A Practical Model for Rough Surface Scattering: The Small Slope Approximation," in *Proceedings of the International Conference on Stochastic Volume and Surface Scattering: Recent Developments in Underwater Acoustics*, 15-17 Dec. 1999, Cambridge, UK (Institute of Acoustics, St. Albans, UK, 1999).
15. D.R. Jackson, D.P. Weinbrenner, and A. Ishimaru, "Application of the Composite Roughness Model to High-Frequency Bottom Backscattering," *J. Acoust. Soc. Am.* **79**, 1410-1422 (1986).
16. K.L. Williams and D.R. Jackson, "Bistatic Bottom Scattering: Model, Experiments and Model/Data Comparison," *J. Acoust. Soc. Am.* **103**, 169-181 (1998).
17. R.F. Gragg and D. Wurmser, "Scattering from Rough Elastic Ocean Floors: Small-Slope Theory and Experimental Data," in *Proceedings of the Environmentally Adaptive Sonar Technologies (EAST) Peer Review*, 8-11 Feb. 2000, Austin, TX (Office of Naval Research Code 321, Arlington, VA, 2000), CD-ROM.
18. R.F. Gragg, D. Wurmser, and R.C. Gauss, "Small-Slope Scattering from Rough Elastic Ocean Floors: General Theory and Computational Algorithm," *J. Acoust. Soc. Am.* **110**, 2878-2901 (2001).
19. D. Wurmser, R.F. Gragg, and R.C. Gauss, "Calculation of Acoustic Scattering from an Elastic Ocean Bottom," *J. Acoust. Soc. Am.* **104**, 1809 (A) (1998).
20. D.M. Drumheller and R.F. Gragg, "Numerical Evaluation of an Integral Found in the Theory of Scattering from Rough Interfaces," NRL/MR/7140-00-8436, Naval Research Laboratory, Washington, DC, April 2000.
21. D.M. Drumheller and R.F. Gragg, "Evaluation of a Fundamental Integral in Rough Surface Scattering Theory," *J. Acoust. Soc. Am.* **110**, 2270-2275 (2001).
22. T. Elfouhaily, B. Chapron, and K. Katsaros, "A Unified Directional Spectrum for Long and Short Wind-Driven Waves," *J. Geophys. Res.* **102**, 15,781-15,796 (1997).
23. H.-H. Essen, "Scattering from a Rough Sedimental Seafloor Containing Shear and Layering," *J. Acoust. Soc. Am.* **95**, 1299-1310 (1994).
24. D.R. Jackson, "APL-UW High-Frequency Ocean Environmental Acoustic Models Handbook," APL-UW TR 9407, Applied Physics Laboratory, University of Washington, Seattle, WA, October 1994.
25. E.L. Hamilton, " V_p/V_s and Poisson's Ratios in Marine Sediments and Rocks," *J. Acoust. Soc. Am.* **66**, 1093-1101 (1979).
26. E.L. Hamilton, "Geoacoustic Modeling of the Sea Floor," *J. Acoust. Soc. Am.* **68**, 1313-1339 (1980).
27. J.K. Fulford, Naval Research Laboratory, Stennis Space Center, MS, private communication, 2000.
28. E.L. Kunz and R.C. Gauss, "Bottom Backscattering Measured Off the Coast of Oregon During the Littoral Warfare Advanced Development 99-3 Experiment," NRL/MR/7140-00-8453, Naval Research Laboratory, Washington, DC, April 2000.
29. A. Turgut, "Inversion of Bottom/Subbottom Statistical Parameters from Acoustic Backscatter Data," *J. Acoust. Soc. Am.* **102**, 833-852 (1997).
30. A.C. Kibblewhite, "Attenuation of Sound in Sediments: A Review with Emphasis on New Low-Frequency Data," *J. Acoust. Soc. Am.* **86**, 716-738 (1989).

31. A. Turgut and T. Yamamoto, "Measurements of Acoustic Wave Velocities and Attenuation in Marine Sediments," *J. Acoust. Soc. Am.* **87**, 2376-2383 (1990).
32. A. Maguer, E. Bovio, W.L.J. Fox, and H. Schmidt, "In Situ Estimation of Sediment Sound Speed and Critical Angle," *J. Acoust. Soc. Am.* **108**, 987-996 (2001).
33. D.D. Ellis and D.V. Crowe, "Bistatic Reverberation Calculations Using a Three-Dimensional Scattering Function," *J. Acoust. Soc. Am.* **89**, 2207-2214 (1991).
34. D.M. Fromm, J.P. Crockett, and L. Bruce Palmer, "BiRASP - The Bistatic Range-dependent Active System Performance Prediction Model," NRL/FR/7140-95-9723, Naval Research Laboratory, Washington, DC, September 1996.
35. R.J. Soukup and P.M. Ogden, "Bottom Backscattering Measured Off the South Carolina Coast During the Littoral Warfare Advanced Development Experiment 96-2," NRL/MR/7140-97-7905, Naval Research Laboratory, Washington, DC, April 1997.
36. R.J. Soukup, "Scattering Measurements and Interface Model Validation for a Rocky Bottom at 2-4 kHz," *J. Acoust. Soc. Am.* **109**, 2300 (A) (2001).
37. D.R. Jackson, P.D. Ingalls, and K-Y Moravan, "100 Hz-10 kHz Bottom Backscatter Model: Generalized Treatment of Sediment Sound Propagation, Sediment Volume Scattering, and Interface-Roughness Scattering," APL-UW TM 1-4, Applied Physics Laboratory, University of Washington, Seattle, WA, April 1994.
38. D.R. Jackson and A.N. Ivakin, "Scattering From Elastic Sea Beds: First-Order Theory," *J. Acoust. Soc. Am.* **103**, 336-345 (1998).
39. A.N. Ivakin and D.R. Jackson, "Effects of Shear Elasticity on Sea Bed Scattering: Numerical Examples," *J. Acoust. Soc. Am.* **103**, 346-354 (1998).
40. D.R. Jackson, "High-Frequency Bistatic Scattering Model for Elastic Seafloors," APL-UW TM 2-00, Applied Physics Laboratory, University of Washington, Seattle, WA, February 2000.
41. R.H. Love, "A Comparison of Volume Scattering Strength Data with Model Calculations Based on Quasisynoptically Collected Fishery Data," *J. Acoust. Soc. Am.* **94**, 2255-2268 (1993).
42. R.W. Nero and M.E. Huster, "Low-Frequency Acoustic Imaging of Pacific Salmon on the High Seas," *Can. J. Fish. Aquat. Sci.* **53**, 2513-2523 (1996).
43. R.W. Nero, C.H. Thompson, and R.H. Love, "Abyssopelagic Grenadiers: The Probable Cause of Low-Frequency Sound Scattering at Great Depths off the Oregon and California Coasts," *Deep-Sea Res.* **44**, 627-645 (1997).
44. R.W. Nero, C.H. Thompson, and R.H. Love, "Low-Frequency Acoustic Measurements of Pacific Hake, *Merluccius Productus*, Off the West Coast of the United States," *Fish. Bull.* **96**, 329-343 (1998).
45. R.C. Gauss, J.M. Fialkowski, D. Wurmser, and R.W. Nero, "New Broadband Models for Predicting Bistatic Surface and Volume Scattering Strengths," in *Proceedings of the Environmentally Adaptive Sonar Technologies (EAST) Peer Review*, 8-11 Feb. 2000, Austin, TX (Office of Naval Research Code 321, Arlington, VA, 2000), CD-ROM.
46. R.C. Gauss, R.W. Nero, and D. Wurmser, "Unifying Acoustic Boundary Scatter Modeling," in *2001 NRL Review*, Naval Research Laboratory, Washington, DC, 2001.

47. D.E. Weston, "Sound Propagation in the Presence of Bladder Fish," in *Underwater Acoustics*, edited by V.M. Albers (Plenum Press, New York, NY, 1967), Vol. 2, Ch. 5, pp. 55-88.
48. C. Feuillade and M.F. Werby, "Resonances of Deformed Gas Bubbles in Liquids," *J. Acoust. Soc. Am.* **96**, 3684-3692 (1994).
49. A.A. Nesterov and S.I. Bazanov, "Vertical Distribution and Behavior of Flying Fishes (*Exocoetidae*)," *J. Ichthyol.* **26**, 159-162 (1986).
50. R.D. Stanley, R. Kieser, B.M. Leaman, and K.D. Cooke, "Diel Vertical Migration by Yellowtail Rockfish, *Sebastes Flavidus*, and Its Impact on Acoustic Biomass Estimation," *Fish. Bull.* **97**, 320-331 (1998).
51. R.M. Alexander, "Buoyancy," in *The Physiology of Fishes* (CRC Press, Boca Raton, 1993), Ch. 3, pp. 75-97.
52. L. Brekhovskikh and Yu. Lysanov, *Fundamentals of Ocean Acoustics* (McGraw-Hill, New York, 1982), Ch. 4, pp. 68-71.
53. P.M. Ogden and F.T. Erskine, "Surface and Volume Scattering Measurements Using Broadband Explosive Charges in the Critical Sea Test 7 Experiment," *J. Acoust. Soc. Am.* **96**, 2908-2920 (1994).
54. D.M. Farmer and S. Vagle, Institute of Ocean Sciences, Sidney, BC, private communication, 1998.
55. C.H. Thompson, R.W. Nero, and R.H. Love, "Volume Scattering on the Littoral Warfare Advanced Development 99-3 Experiment," NRL/MR/7180-01-8255, Naval Research Laboratory, Stennis Space Center, MS, 2001.
56. A. Turgut, Naval Research Laboratory, Washington, DC, private communication, 2001.
57. O. Diachok, "Effects of Absorptivity Due to Fish on Transmission Loss in Shallow Water," *J. Acoust. Soc. Am.* **105**, 2107-2128 (1999).
58. S.T. McDaniel, "Sea Surface Reverberation: A Review," *J. Acoust. Soc. Am.* **94**, 1905-1922 (1993).
59. R.C. Gauss and J.M. Fialkowski, "A Broadband Model for Predicting Bistatic Surface Scattering Strengths," in *Proceedings of the Fifth European Conference on Underwater Acoustics*, edited by M.E. Zakharia et al., 10-13 July 2000, Lyon, France (European Commission, Luxembourg, 2000), Vol. 2, pp. 1165-1170.
60. R.C. Gauss and J.M. Fialkowski, "Estimating Surface Scattering Strengths Using Remotely-Sensed Oceanographic Variables," in *Proceedings of the 29th Meeting of The Technical Cooperation Program Maritime Systems Group Technical Panel Nine (TTCP MAR TP-9)*, 6-10 Nov. 2000, Auckland, New Zealand (Defence Operational and Technology Support Establishment, Auckland, New Zealand, 2000).
61. R.C. Gauss, E.I. Thorsos, F.S. Henyey, and J.M. Fialkowski, "The Dependence of Low-Frequency Surface Scattering on Remotely-Sensed Oceanographic Variables," *J. Acoust. Soc. Am.* **108**, 2585 (A) (2000).
62. P.A. Hwang, D.W.C. Wang, E.J. Walsh, W.B. Krabill, W. Wright, and R.N. Swift, "Airborne Measurements of the Directional Wavenumber Spectra of Ocean Surface Waves. Part 2: Directional Distribution," *J. Phys. Oceanogr.* **30**, 2768-2787 (2000).
63. "Coastal and Marine Applications of Wide Swath SAR," special issue of the *Johns Hopkins APL Tech. Dig.* **21** (1), edited by R.C. Beal and W.G. Pichel (2000).

64. R.P. Chapman and J.H. Harris, "Surface Backscattering Strengths Measured with Explosive Sound Sources," *J. Acoust. Soc. Am.* **34**, 1592-1597 (1962).
65. M. Nicholas, P.M. Ogden, and F.T. Erskine, "Improved Empirical Descriptions for Acoustic Surface Backscatter in the Ocean," *IEEE J. Ocean Engr.* **23**, 81-95 (1998).
66. K.E. Gilbert, "A Stochastic Model for Scattering from the Near-Surface Oceanic Bubble Layer," *J. Acoust. Soc. Am.* **94**, 3325-3334 (1993).
67. R.C. Gauss and J.M. Fialkowski, "A New, Semi-Empirical Model for Predicting Bistatic Surface Backscattering Strengths," in *Collected Papers of the 137th Meeting of the Acoustical Society of America*, 14-19 Mar. 1999, Berlin, Germany (Acoustical Society of America, 1999), CD-ROM.
68. E.I. Thorsos, D.R. Jackson, and K.L. Williams, "Modeling of Subcritical Penetration in Sediments Due to Interface Roughness," *J. Acoust. Soc. Am.* **107**, 263-277 (2000).

